Earth's Future

RESEARCH ARTICLE
10.1029/2025EF007294

Special Collection:
Forcing, response, and impacts of coastal storms in a changing climate

# Global Warming Enhances Tropical Cyclone–Induced Extreme Precipitation in the Arabian Sea: Insights From Convection-Permitting Model Experiments

**Akash Pathaikara[1], Minkyu Lee[2], Seung-Ki Min[1,3], Dong-Hyun Cha[4], Doo-Sun R. Park[5], Soon-Il An[1,6], Mathew K. Roxy[7], and Raju Attada[8]**

[1]Division of Environmental Science and Engineering, Pohang University of Science and Technology, Pohang, South Korea, [2]Renewable Energy Big Data Laboratory, Korea Institute of Energy Research, Daejeon, South Korea, [3]Institute for Convergence Research and Education in Advanced Technology, Yonsei University, Seoul, South Korea, [4]Department of Civil, Urban, Earth and Environmental Engineering, Ulsan National Institute of Science and Technology, Ulsan, South Korea, [5]Department of Earth Science Education, Kyungpook National University, Daegu, South Korea, [6]Department of Atmospheric Sciences, Yonsei University, Seoul, South Korea, [7]Centre for Climate Change Research, Indian Institute of Tropical Meteorology, Pune, India, [8]Department of Earth and Environmental Sciences, Indian Institute of Science Education and Research (IISER) Mohali, Mohali, India

**Abstract** The frequency and intensity of extreme weather events have risen with climate change, affecting multiple sectors worldwide. This study examines the influence of anthropogenic warming on intense tropical cyclones (TCs) over the Arabian Sea using convection-permitting simulations with the Weather Research and Forecasting (WRF) model. In particular, we provide the first quantitative assessment of the impact of anthropogenic forcing on recently observed TC-induced extreme rainfall. Human-induced changes were assessed through two experiments: all forcings (ALL) and natural forcings only (NAT). Anthropogenic warming "delta" patterns of sea surface temperature, relative humidity, and air temperature were derived from CMIP6 models and applied in WRF under a pseudo-global warming framework. Three major TCs—Ockhi (2017), Kyarr (2019), and Maha (2019)—were simulated, and the model reproduced their tracks, intensities, and rainfall with high fidelity. Comparison of ALL and NAT runs shows a clear anthropogenic signal: TC-induced total and extreme rainfall both increases, linked to stronger vertical motion and greater moisture availability that enhance latent heat release and deep convection. Furthermore, there is a statistically significant expansion in the area experiencing extreme rainfall by ∼16%–34%, and an enhanced intensity of extreme rainfall by ∼4%–12% under anthropogenic warming. Additional differences in vertical thermal profiles and warm-core structures further highlight the impact of human-induced climate change on TC dynamics.

**Plain Language Summary** The North Indian Ocean cyclone basin is divided into two regions: the Arabian Sea and the Bay of Bengal. Previous studies suggest that global warming has made the Arabian Sea more prone to intense cyclones. Heavy rainfall and strong winds are the main drivers of cyclone-related destruction. However, the role of human influence on cyclone-induced rainfall over the Arabian Sea remains poorly understood. This study examines how global warming alters the intensity and spatial extent of cyclone-associated rainfall. Results show increases in average rainfall, extreme rainfall, and the area affected by heavy rainfall, attributable to human-induced climate change. Stronger mid-tropospheric upward motion and greater lower-tropospheric moisture are the primary mechanisms behind these changes. Overall, this study underscores how human influence is amplifying cyclone destructiveness and highlights the urgent need to reduce greenhouse gas emissions for a sustainable future.

**Key Points:**

- Global warming impacts on intense tropical cyclones are investigated using convection-permitting simulations
- Anthropogenic warming enhances tropical cyclone-induced extreme rainfall and its spatial extent
- Increased moisture and stronger upward motion contribute to the rainfall intensification and spatial shift

**Supporting Information:**

Supporting Information may be found in the online version of this article.

**Correspondence to:**

S.-K. Min,
skmin@postech.ac.kr

**Citation:**

Pathaikara, A., Lee, M., Min, S.-K., Cha, D.-H., Park, D.-S. R., An, S.-I., et al. (2026). Global warming enhances tropical cyclone–induced extreme precipitation in the Arabian Sea: Insights from convection-permitting model experiments. *Earth's Future*, *14*, e2025EF007294. https://doi.org/10.1029/2025EF007294

Received 9 SEP 2025
Accepted 18 JAN 2026

**Author Contributions:**

**Conceptualization:** Seung-Ki Min
**Data curation:** Akash Pathaikara
**Formal analysis:** Akash Pathaikara
**Funding acquisition:** Seung-Ki Min
**Investigation:** Akash Pathaikara
**Methodology:** Akash Pathaikara, Minkyu Lee
**Resources:** Minkyu Lee
**Supervision:** Seung-Ki Min
**Validation:** Minkyu Lee, Seung-Ki Min



## 1. Introduction

Tropical cyclones (TCs) and their devastating impacts pose a persistent threat to coastal nations, causing widespread human and economic losses and disrupting all sectors of life. The North Indian Ocean (NIO) is one of the major TC basins, consisting of two sub-basins, the Arabian Sea (ARB) and the Bay of Bengal, with particular significance due to its densely populated coastlines. The historical cyclone-landfalling events were potentially devastating in terms of both human life and economic loss (Kikuchi et al., 2009; Lin et al., 2009; Mohanty et al., 2014, 2015; Webster, 2008). An extremely severe cyclonic storm such as Kandla (1998), recorded a death toll of 1173 (Mohapatra & Sharma, 2025). In the case of cyclone Ockhi (2017), forecasts failed to predict the rapid

**Writing – original draft:** Akash Pathaikara, Minkyu Lee, Seung-Ki Min
**Writing – review & editing:** Dong-Hyun Cha, Doo-Sun R. Park, Soon-Il An, Mathew K. Roxy, Raju Attada

intensification, and the cyclone impacted the entire west coast of India and Sri Lanka, affecting more than 220,000 people (EM-DAT, 2008; Singh et al., 2020). In addition to these social impacts, the thermodynamic factors such as moist static energy (MSE) and tropical cyclone heat potential (TCHP) in ARB are becoming more conducive for the formation and intensification of intense TCs in response to anthropogenic greenhouse gas emissions (Pathaikara et al., 2025).

Moving on to the simulation studies, the Weather Research and Forecast (WRF) proved to work well with convection-permitting schemes over the NIO, simulating Bay of Bengal cyclones with satisfactory capturing of track and intensity (Mohan et al., 2022). Studies have indicated that due to the deepening of the TC core and enhancement of latent heat, cyclones such as Phailin (2013) formed over the Bay of Bengal will be more intense and larger in the future with the pseudo-global warming (PGW) method (Mittal et al., 2019). Jyoteeshkumar Reddy et al. (2021) also used the PGW framework with WRF over the Bay of Bengal and reported that individual TCs can jump to the next category in the far future—high-emission scenarios. Here, they defined the future warming pattern of the NIO from a single member, CCSM4 of CMIP5. However, over ARB, the simulation studies of TCs with PGW approaches are fewer compared with the Bay of Bengal. With the real-world conditions, WRF simulations of TC Shaheen (2021) and Biparjoy (2023) over ARB demonstrate the underestimation of intensity, yet they adequately simulate the precipitation in the regions along the track (Karami & Khansalari, 2024). This underestimation of the intensity of intense TCs in WRF simulations is furthermore observed in the case of TC Chapala (2015) and Megh (2015) with real-world runs (Kumar et al., 2020). The WRF simulation of Very Severe Cyclonic Storm Ockhi (2017) over the ARB further highlights this limitation, revealing discrepancies in the spatial extent of rainbands (Mukherjee & Ramakrishnan, 2023). However, it also demonstrates WRF's capability to capture the extreme rainfall intensity during the cyclone's mature stage.

Despite the existence of studies that simulate TCs over ARB, none of these have been approached using a PGW framework for quantifying human-caused impacts on the observed TCs. For instance, Ranji et al. (2022) used the PGW framework and WRF with a suite of CMIP5 models to project future changes in the historical TCs Gonu (2007), Phet (2010), and Ashobaa (2015) that formed over the ARB. Their findings indicate that the sea surface temperature (SST) and air temperature predominantly influence the track and intensity of these storms. Apart from intensity and track, no mention was made of the TC-induced rainfall and extreme rainfall, which is a major part that needs to be addressed. In addition to Ranji et al. (2022) and Jyoteeshkumar Reddy et al. (2021), the present study investigates the impact of anthropogenic forcings on the increased TC-induced rainfall intensity and provides the plausible physical mechanism behind it. In contrast to the approach adopted by Jyoteeshkumar Reddy et al. (2021), who defined the warming pattern from a single model, we have designed the PGW experiment using all available CMIP6 models to minimize the uncertainty of a single model. Furthermore, all the above-mentioned studies employ the CMIP5 models to derive patterns of climate change, which have been shown to exhibit larger SST bias over major ocean basins in comparison to CMIP6 (Farneti et al., 2022; Zhang et al., 2023). To elaborate more specifically, this better representation of the SST-mean state in CMIP6 over ARB in the ON season (Lyon, 2022) signifies a methodological advancement of this study.

In a similar vein, Lee et al. (2023) utilized the PGW framework to study TCs formed over the northwestern Pacific, deriving anthropogenic warming patterns from CMIP6 models. Their findings indicate an expansion of the area experiencing extreme rainfall of 16%–37% attributable to human influence. However, the researchers have not demonstrated the statistical significance of the results, nor have they addressed the changed vertical structure of TC. On top of this, the present study is concerned with the changing horizontal and vertical patterns of variables, as well as measuring the statistical significance of results. The observed phenomena—human-induced expansion of the Indo-Pacific warm pool (Weller et al., 2016), accelerated thermal preconditioning of the Arabian Sea warm pool (Pathaikara et al., 2025), and the most pronounced warming trend of SST of ARB (Roxy et al., 2024)—keep ARB as a high-alert region necessitating in-depth studies. The considerable increase in the projected population in the rim countries of ARB coasts (Harrington et al., 2018) substantiates the quantification of the anthropogenic influence on the destructiveness potential of TCs in the region.

A deep dive into the oceanic factors reveals that both SST and TCHP (Leipper & Volgenau, 1972) play a major role in the intensification of TCs, with additional weightage to TCHP (Evans, 1993; Gray, 1979; Wada, 2015; Wada & Usui, 2007; Wang & Zhou, 2008). In addition to this, in the tropical regions of warmer SST, the atmospheric column will be more humid, which is due to the extensive convective moistening (Bretherton et al., 2004). The relative humidity (RH) and total precipitable water in the atmosphere strongly influence TC-

induced rainfall (Guzman & Jiang, 2021; Hill & Lackmann, 2009; Matyas, 2010). The moisture supply to the TC system is primarily through the low-level atmospheric convergence and intensification through the latent heat transfer at the sea surface (Braun, 2006; Emanuel, 1986; Yang et al., 2011). Another index for representing the atmospheric instability is MSE, which is closely related to the formation and intensification of intense TCs (Emanuel, 1994; Marquet, 1993; Pathaikara et al., 2025).

Given the absence of PGW framework studies utilizing the WRF and the suite of CMIP6 (Coupled Model Intercomparison Project Phase 6) models over ARB, this study seeks to undertake a simulation analysis of selected TCs over ARB. We considered the post-monsoon season (October–December) as a more suitable season than pre-monsoon (March–May), since it shows an increasing trend of background factors such as RH, MSE, potential intensity, and genesis potential index, which is more conducive to intense TCs (Abhinav et al., 2025; Deshpande et al., 2021). With this in mind, we selected the three most intense TCs formed over ARB from 2016 in the post-monsoon season: Kyarr (2019), Maha (2019) and Ockhi (2017) (Table S1 in Supporting Information S1). There are several studies that typify the track characteristics of ARB TCs. An analysis of the Joint Typhoon Warning Center (JTWC) observation data set shows 74.6% of the tracks of TCs over ARB are oriented in the west and northwest direction (Xiao-ting et al., 2020). Recent studies using the JTWC data set also observed the west or northwestward trajectory of tracks (Jayasekara et al., 2024; Najah et al., 2025). Another predominant behavior is the north-to-northeast recurving of tracks (Kabir et al., 2022). Considering these findings, the climatological variability is also represented by the three selected TCs under consideration: Kyarr (westward-moving), Ockhi (northwestward-moving) and Maha (northwestward-then-eastward-curving).

## 2. Data and Methods

### 2.1. Observations

The 6-hourly data set provided by JTWC (Chu et al., 2002) and India Meteorological Department (IMD) was utilized to obtain observed central sea-level pressure (CSLP) and maximum sustained wind (VMAX) of TCs. The 6-hourly accumulated precipitation is calculated from the Tropical Rainfall Measuring Mission-3B42 version 7 (TRMM) (Huffman et al., 2007) and 30-min Integrated Multi-satellite Retrievals for GPM (IMERG) (Hou et al., 2014).

### 2.2. WRF Model Configuration

The simulation of TCs was conducted utilizing the WRF version 4.0, employing the ERA5 reanalysis data set (Hersbach et al., 2020) as the atmospheric initial condition and boundary condition. The SST input was derived from the National Oceanic and Atmospheric Administration's Daily Optimum Interpolation Sea Surface Temperature version 2.0. The complete experiments have been performed with an enabled convection-permitting scheme, using a single domain of 3 km resolution with 1787 × 982 grid points (Figure S1 in Supporting Information S1) in the horizontal and 50-sigma levels in the vertical, reaching up to 50 hPa at the top of the atmosphere. Cumulus scheme has been disabled in order to allow explicit convection in the model. The microphysics, shortwave and longwave radiation, and the planetary boundary layer schemes are set to the WRF single-moment 6-class (Hong & Lim, 2006), the Rapid Radiative Transfer Model for the General Circulation Model (Iacono et al., 2008), and the Yonsei University scheme (Hong, 2010; Hong & Lim, 2006), respectively. The spectral nudging technique was applied above 10 lowest sigma levels for the atmospheric temperature and horizontal wind in all the experiments to simulate tracks realistically despite the initial conditions and boundary conditions being perturbed (Cho et al., 2022; Storch et al., 2000). Spectral nudging is used here to simulate the track and intensity more realistically, which is essential to compare the rainfall pattern with observation and draw conclusions (Gutmann et al., 2018; Mori et al., 2014; Takayabu et al., 2015). It is difficult to extract the influence of anthropogenic warming patterns on the direction of track and translation speed of TCs in this experimental design. Conversely, the well-synchronized track is a necessity to analyze the change in TC-induced rainfall and extreme rainfall, with particular reference to the TC system.

### 2.3. ALL and NAT Experiments

The study focuses on the three most intense TCs that occurred over the ARB during the post-monsoon season in the post-2016 period. The first one is the most deadly-Ockhi (2017), having a lifetime maximum intensity (LMI) recorded 100 knots, causing over 800 casualties in India and Sri Lanka (EM-DAT, 2008). It intensified to a

Cyclonic Storm (CS category; VMAX ≥34 knots) on 29-11-2017:12 hr and weakened to a deep depression (VMAX <34 knots) on 05-12-2017:06 hr before landfall at Coordinated Universal Time. The second and third TCs are Kyarr (2019) and Maha (2019), which recorded LMI of 135 and 110 knots, respectively. Kyarr is the strongest super cyclonic storm (VMAX ≥120 knots) formed over ARB in the post-monsoon season (Akhila et al., 2022). The commencement and cessation times of the simulation are designated as the observed times at which the corresponding system transitions to the CS stage and weakens below the CS stage, respectively. The initialization time of the model was determined by referring to successful WRF simulations over the western North Pacific with PGW approach (Kim et al., 2024; Lee et al., 2023; Olschewski et al., 2024). The other models, such as the GFDL hurricane model, have also adopted this same method for more precise simulation of events (Knutson et al., 2015, 2022). A comprehensive description of TCs, inclusive of the simulation time, is provided in Table S2 of Supporting Information S1. The location of simulated TCs and associated CSLP is obtained by marking the geographic coordinate of minimum sea-level pressure within a 500 km radius of observed CSLP and its value at the corresponding time. Simulated VMAX is defined as the maximum 10 m wind speed determined within a 500 km radius, consistent with previous studies (Michalek et al., 2024; Moon et al., 2021). According to Knaff et al. (2015), a radial distance of 500 km represents the outer scale of a TC, encompassing its broad radial structure. Thus, searching for VMAX within a 500 km radius is unlikely to miss TC-related winds, particularly for large, asymmetric, or transitioning storms. Radial distances of 550–600 km fall within the outer cloud bands of TCs (Englehart & Douglas, 2001) can therefore be considered part of the TC system. Moreover, a 500 km radius has been widely adopted to distinguish TC-induced rainfall from other weather systems (Jiang et al., 2011; Lonfat et al., 2007; Nogueira & Keim, 2010). Considering the employment of advanced data validation techniques, particularly for strong TCs with intensities exceeding 100 knots (Ricciardulli et al., 2023), the JTWC database is referred to as the observed track in the above process.

The present study considers the impact of enhanced thermodynamic components on the behavior of TCs. To align with the objectives of the study, it was decided to perturb the variables SST, skin temperature, RH (across all levels) and atmospheric temperature corresponding to the anthropogenic warming pattern. The selection of these variables is informed by prior studies that employed a similar approach over different regions, including South Korea and the Philippines (Delfino et al., 2023; Lee et al., 2023). Previous studies have shown that including horizontal winds in the PGW framework can cause unwanted effects on cyclogenesis, such as random changes in windshear and alterations in the track (Olschewski & Kunstmann, 2024; Patricola & Wehner, 2018). Therefore, we excluded the horizontal wind components from the PGW framework. To calculate the anthropogenic changes in the aforementioned variables, 10 CMIP6 models were utilized (Table S3 in Supporting Information S1). Adding the response of variables in the general circulation model to the present-day boundary conditions is the usual method of PGW framework (Bacmeister et al., 2018; Knutson et al., 2015; Murakami, Mizuta, & Shindo, 2012, Murakami, Wang, et al., 2012; Wehner et al., 2018). Here, the anthropogenic warming pattern (hereafter "delta pattern") was calculated by subtracting the multi-model mean of the hist-NAT experiments (natural-only forcing) from the historical experiment (anthropogenic plus natural forcing) in the period 2011–2020 for the post-monsoon season. For example, the mean anthropogenic SST warming that resulted over the ARB was nearly +1°C in the OND season (Figure 1g). To get the delta patterns for individual TCs, we performed the daily interpolation of CMIP6 monthly data to find background variables on each date if TC dates are extended from 1 month to another. We have implemented this technique, which obtains a smoothly varying daily seasonal cycle of delta patterns, referring to the previous studies (Hauser et al., 2017; Lauer et al., 2013). As demonstrated in the studies by Deser et al. (2007) and Lan et al. (2022), variables like SST and skin temperature can be successfully interpolated in this method. Also note that our delta patterns are obtained from multi-model averages, further reducing internal variability noise. The historical experiment was constructed by integrating historical simulations (2011–2014) with Shared Socioeconomic Pathway 2–4.5 (SSP2-4.5) simulations (2015–2020), which is a widely used method for extending the CMIP historical simulations beyond 2014 (Gillett et al., 2016, 2025; Ribes et al., 2021). The ensemble mean of each CMIP6 model was calculated across all available ensemble members before constructing the multi-model mean; aiming to ensure equal weightage of each model. The WRF runs with a natural-only forcing environment (NAT) are designed by subtracting delta patterns of the above-mentioned variables from the initial and boundary conditions of real-world runs (ALL). In NAT runs, the greenhouse gas concentrations are also set to pre-industrial levels (i.e.; $CO_2$, $CH_4$, and $N_2O$ at 284.3 ppm, 808.2, and 273.0 ppb, respectively) (Meinshausen et al., 2017). In this study, the values above 150 mm per 6 hr are defined as extreme rainfall. The unit of rainfall used in this study is mm per 6 hr, denoted as "mm 6 $hr^{-1}$" here

10.1029/2025EF007294

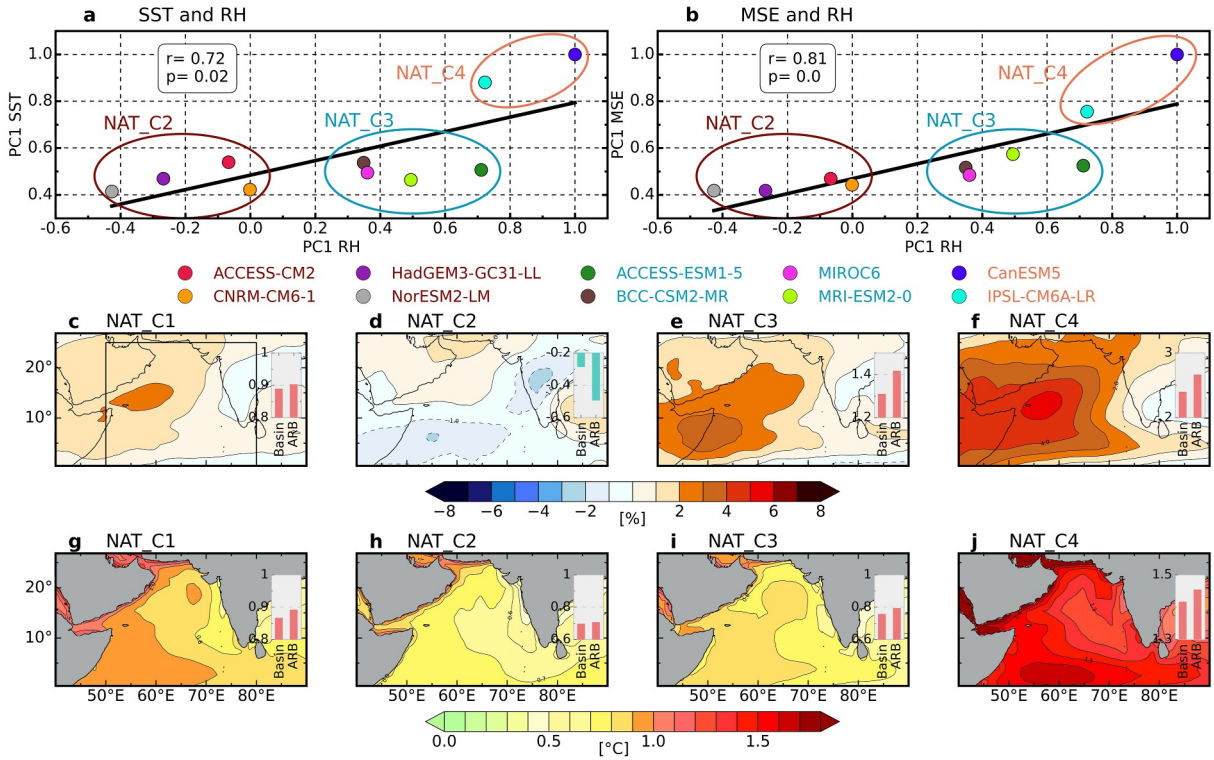


**Figure 1.** Clustering of models and delta patterns. (a) Scatter plot of the first principal component (PC1) from the delta pattern of sea surface temperature (SST) and RH in OND season of each model. The corresponding clustering of models is represented in circles. Black solid lines indicate the linear regression lines with correlation coefficient (*r*-value) and corresponding *p*-value indicated. (b) Same as (a) but using PC1 of moist static energy and RH. (c–f) RH delta pattern of clusters NAT_C1 to NAT_C4. The bar plot inside each subplot represents the area average of the delta pattern in the entire basin and ARB, where the ARB domain is indicated as a black box in (c). In panels (g–j) same as (c–f) but for the variable SST.

onwards. We equally split the simulation time of each TC into three to do an in-depth analysis and make the results more reliable in all stages of the storm (Figure S1 in Supporting Information S1).

To ensure the reliability of results, ALL runs are performed using five ensembles: ALL_minus12h, ALL_minus6h, ALL_plus0h, ALL_plus6h, and ALL_plus12h. The suffix "minus12h" means the simulation initializes 12 hr before the observed time when the TC enters the CS stage; the other ensembles follow the same pattern. To consider the inter-model uncertainty in delta patterns, the NAT runs are also divided into four ensembles using delta patterns of the cluster of models NAT_C1, NAT_C2, NAT_C3, and NAT_C4 (Figure 1). The multi-model mean of all 10 models is considered as C1. This classification is carried out by examining the first principal component (PC1) of SST, the mean relative humidity of the vertical column of 700–500 hPa, and MSE (Emanuel, 1994). The Empirical Orthogonal Function (EOF) analysis is applied to the delta pattern across 10 models, and the first EOF of delta SST and RH explains 88.35% and 66.29% of the inter-model variability in the domain, respectively (Figure S2a and S2b in Supporting Information S1). Here, cluster NAT_C4 represents the highest anthropogenic delta pattern (Figures 1a and 1b). Above the other clusters, NAT_C1 is utilized to derive the primary results, as it represents multi-model means.

## 3. Results

### 3.1. Model Performance for TC Intensity and Precipitation

Figure 2 shows the ability of convection-permitting models to capture the observed intensity and track of TCs while considering the VMAX and CSLP as indicators of intensity. The ALL_plus0h (ALL) underestimates the intensity of Kyarr and Maha by about 25 and 23 kts, respectively, compared to JTWC (Figures 2a and 2b). It should be noted that the rapid intensification experienced by both TCs is not captured by the model, as reported by previous studies (Karami & Khansalari, 2024; Kumar et al., 2020). The beginning hours of the simulation overestimate the intensity, even though it realistically captures intensity in the decaying period of each storm

10.1029/2025EF007294

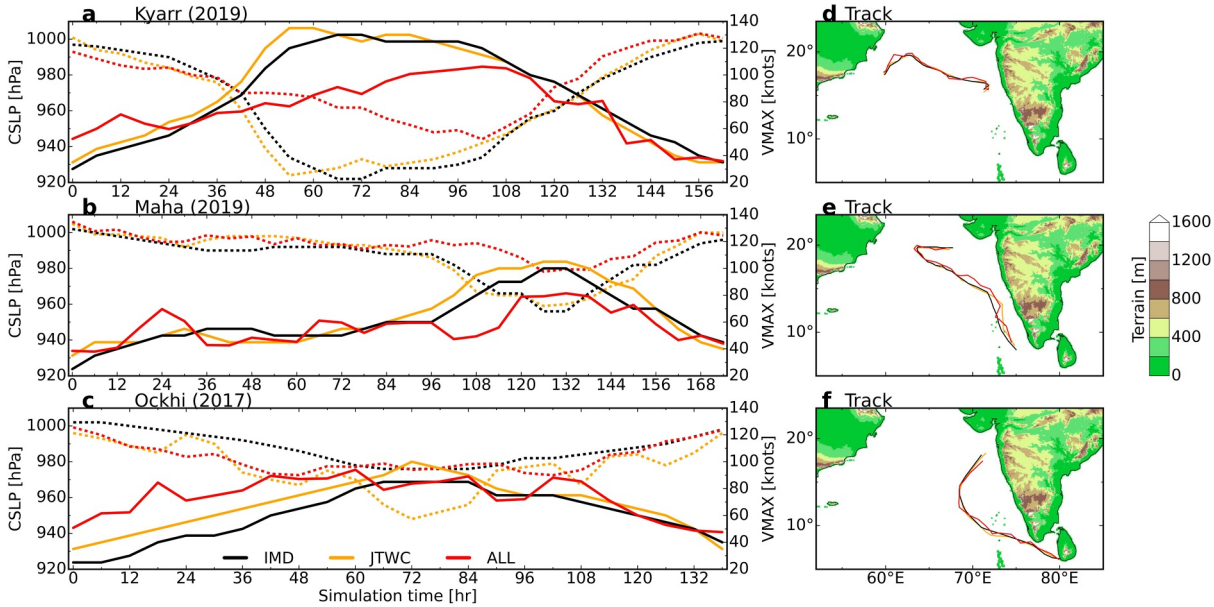


**Figure 2.** Simulated track, VMAX and central sea-level pressure (CSLP) against observations. (a) Simulated and observed evolution of VMAX (continuous line) and CSLP (dashed line) with simulation time of TC Kyarr. (d) Simulated and observed track of Kyarr from India Meteorological Department (black), Joint Typhoon Warning Center (orange), and ALL (red) with terrain height (shaded over land). In panels (b), (e) and (c), (f) are the same as (a, d), but for TCs Maha and Ockhi, respectively.

(Figures 2a–2c). The intensity of Ockhi is captured in ALL after 60 hr, but there is still a significant discrepancy between JTWC and IMD in the estimation of maximum intensity. Overall, the average intensity is simulated reasonably. As a result of spectral nudging, the observed tracks of the three TCs are reproduced with very small errors (Figures 2d–2f, Table S4 in Supporting Information S1). The inter-ensemble agreement of the simulations in intensity and track recreation makes the results more reliable (Figure S3 in Supporting Information S1).

The precipitation induced by TCs causes major disasters. The widespread extreme rainfall caused by Ockhi on the coasts of India and Sri Lanka caused huge economic and life loss to these countries (EM-DAT, 2008). It is important to assess the fraction of contribution by anthropogenic global warming to the extreme rainfall induced by these TCs. In the current study, we optimized the area for area-averaged calculations from 500 to 300 km, given that TCs in ARB are smaller in size. Figures 3a–3c shows that the average rainfall experienced within a 300 km radius of the storm is well simulated by ALL compared to the TRMM. At the same time, IMERG shows the highest amount of rainfall in Kyarr and Maha. In the case of Ockhi and Maha, IMERG recorded more rainfall at the beginning of the storm, but later it aligns with TRMM and ALL (Figures 3b and 3c). The large amount of rainfall at the beginning hours of these TCs aligns perfectly at the beginning of the storm, and their tracks are close to Sri Lanka and India at this stage (Figures S1b and S1c in Supporting Information S1). It is important to note that Sri Lanka and the Southern peninsular India suffered significant human and Economic loss at this initial phase of the storm. The probability density function (PDF) is used to represent the fraction of grid points experiencing 6-hourly rainfall quantity inside a 300 km radius of TC. We have considered TC-induced rainfall as the rainfall inside the 300 km radius and recorded above 10 mm 6 $hr^{-1}$ only. To estimate the PDF, we exclusively considered TC-induced rainfall. A very close agreement between ALL and IMERG is observed in the integrated area of rainfall irrespective of light or heavy precipitation in all three TCs (Figures 3d–3f). The capability of IMERG in capturing large-scale features of precipitation compared to TRMM, over the NIO, along with its overestimation compared to the in situ measurements, was explained in previous studies (Pradhan & Markonis, 2023; Prakash et al., 2018). On the other side, the high rainfall rates associated with TCs over this region are underestimated by TRMM by about 25%–50% relative to precipitation radar (PR2A25) (Prakash et al., 2012). Similarly, preceding studies comparing these data sets in the context of TC-induced rainfall reveal that IMERG appears to outperform TRMM in both areas of accumulated rainfall and extreme rainfall (Yuan et al., 2021). Furthermore, IMERG captures an additional 10% extreme events compared to TRMM in a global-scale analysis as well, with gauge-based measurements as a reference (Behrangi et al., 2016). While entering the TC system, IMERG was

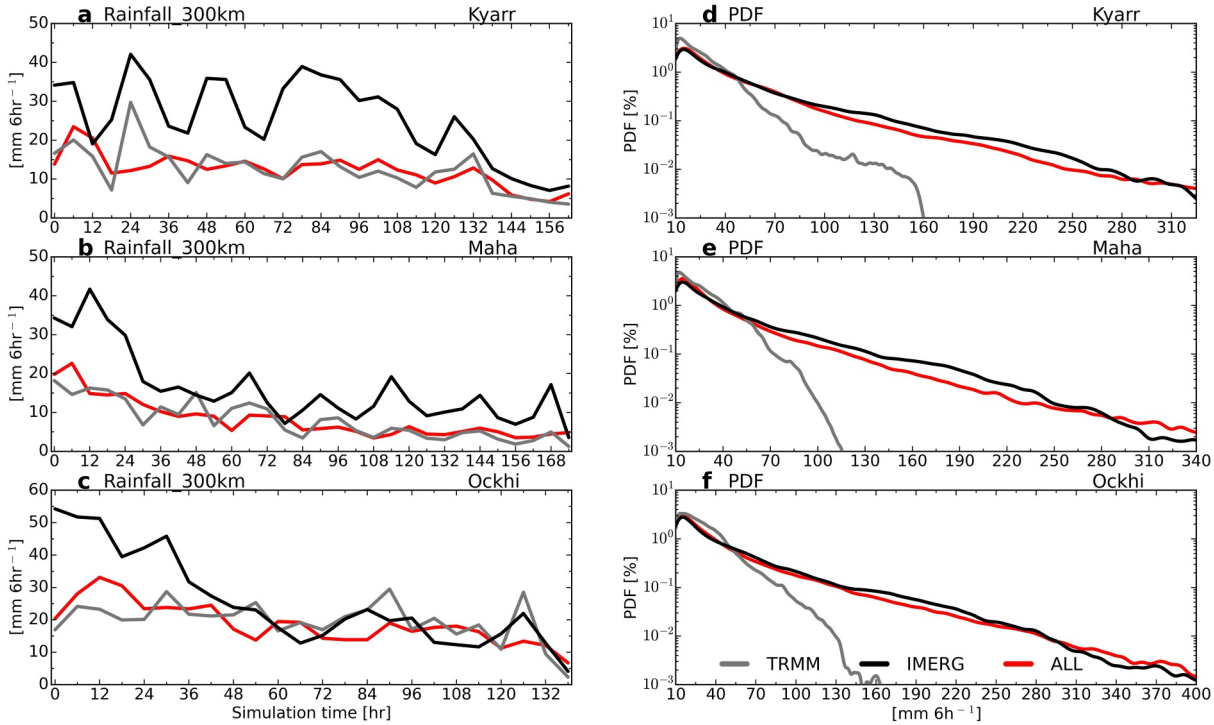


**Figure 3.** Simulated versus observed precipitation. (a) Observed and simulated average precipitation within a 300 km radius around the TC center of TC Kyarr against simulation time. (d) The probability density function (PDF) of precipitation within a 300 km radius around the TC center of TC Kyarr. Precipitation <10 mm 6 $hr^{-1}$ is not considered for PDF estimation. In panels (b), (e) and (c), (f) are the same as (a, d), but for TCs Maha and Ockhi, respectively.

identified as one of the data sets widely used owing to its ability to give the structural information within a 200 km radius of TC (Durden, 2024; Yang et al., 2024). However, TRMM captures TC-induced rainfall with low to moderate intensity. Lee et al. (2023) found a similar underestimation of TRMM in the heavier precipitation regions over the western North Pacific. In summary, the average precipitation within a 300 km radius is overall matched to TRMM, and the PDF showed similar results to IMERG regardless of the TC.

Hence, there is an underestimation of simulated VMAX (Figures 2a–2c), the intensity change at each step of the TC was examined against the rainfall bias within a 200 km radius (Figure S4 in Supporting Information S1) to assess the effect of intensity bias on rainfall. The Figure S4 in Supporting Information S1 indicates that the TC intensity is underestimated in the majority of the time steps across all TCs, with the exception of Ockhi. It is important to note that, during the time steps when the TC was under RI, both rainfall and VMAX were largely underestimated in Kyarr and Maha, with some exceptions in Kyarr (Figures S4a–S4j in Supporting Information S1). In contrast, Ockhi simulations resulted in overestimation of VMAX and exhibited positive or near-zero rainfall anomalies during the RI stage, which is discussed in Figure 2. However, a significant relationship between the bias in inner-core rainfall and VMAX was not observed across the storms and simulations, except for the ALL_minus12 h and ALL_plus12 h simulations of Kyarr. Consequently, it is not feasible to establish a substantial link between VMAX and inner-core rainfall from this limited analysis.

### 3.2. Human Influence on TC Rainfall

The comparison between the precipitation and extreme precipitation simulated in ALL and NAT runs gives further insights into the influence of anthropogenic warming on TC-induced precipitation (Figure 4). There is no discrepancy between ALL and NAT runs in the fraction of grids possessing TC-induced rainfall with lower intensity in all three TCs. However, when coming to heavy rainfall values, ALL simulations exhibited higher PDF values compared to the NAT simulations in Kyarr and Maha (Figures 4a and 4b). The increased area experiencing the heavy rainfall is quite different from those with light rainfall, potentially exerting the catastrophic effects. In the case of Kyarr, this disparity starts from 310 mm 6 $hr^{-1}$. Conversely, in Maha, it is evident from 210 mm 6 $hr^{-1}$ onwards that the impact of anthropogenic warming is pronounced. Even though it is less visible in the case of

10.1029/2025EF007294

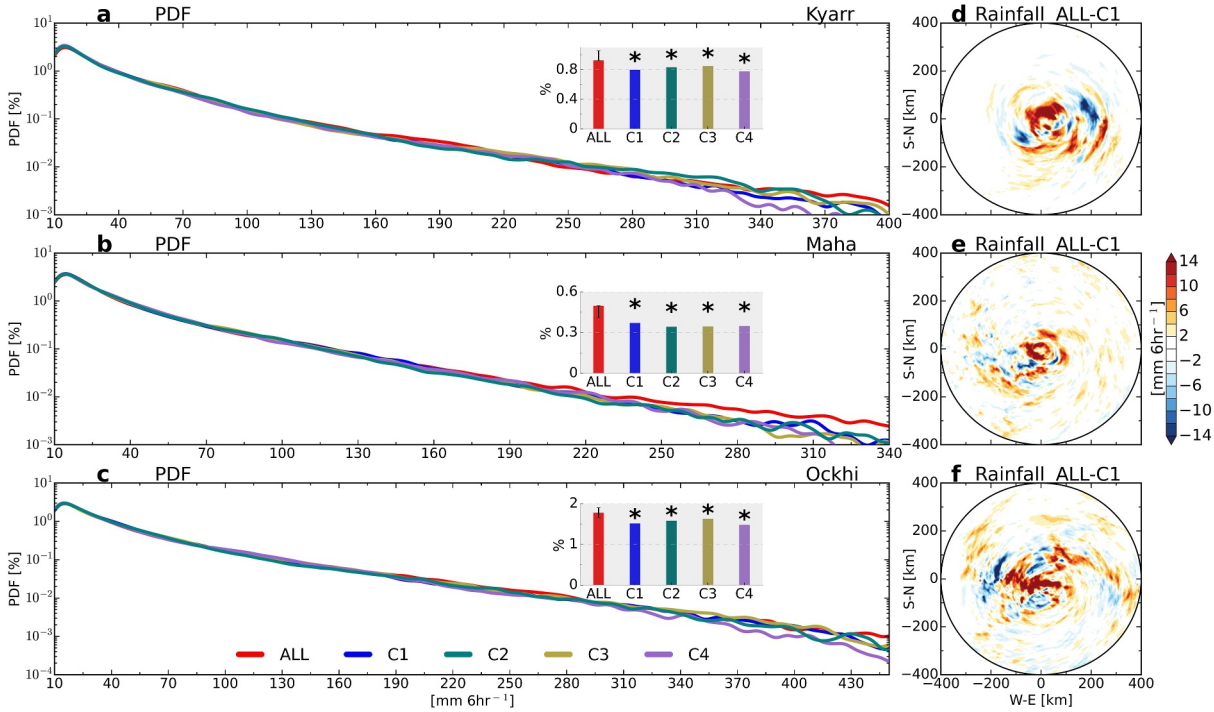


**Figure 4.** Comparison of heavy precipitation in different runs. Panel (a) probability density function (PDF) of rainfall experienced within a 300 km radius around the TC center of TC Kyarr. Precipitation <10 mm 6 hr $^{-1}$ is not considered for PDF estimation. The bar plot inside shows the percentage of grids experiencing heavy precipitation (≥150 mm 6 hr$^{-1}$) for each scenario. The red bar shows ALL_plus0h and error bars indicate the lower and upper limits of the ensemble runs. Conducted the one-sample *t*-test among ALL (5 members) and NAT (one member) and added "*" marks on top of the NAT bars, showing significance at a level of 5%. In panels (b) and (c) are same as (a) but for TCs Maha and Ockhi respectively. (d–f) Spatial pattern of precipitation difference (ALL minus NAT_C1) averaged in the entire period for TC Kyarr, Maha, and Ockhi, respectively.

Ockhi, NAT_C4 (the cluster having the largest delta pattern) shows this impact of anthropogenic warming pattern from 310 mm 6 hr$^{-1}$ onwards.

The ALL simulation demonstrates a greater percentage of the area experiencing extreme precipitation (>150 mm 6 hr$^{-1}$) compared to the NAT_C1- NAT_C4 clusters (Figuure 4a bar plot), indicating that ALL records 16% larger area than NAT_C1 for the TC Kyarr, which is significant at 1% level (Table S5 in Supporting Information S1). A one-sample *t*-test was conducted to identify the level of significance of the results among ALL (five members) and NAT (one member); the values in the bar plot with p-values are specified in Table S5 of Supporting Information S1. A similar outcome was observed in the Maha and Ockhi cases, with a significant (at 1%) excess area experiencing extreme rainfall in ALL compared to NAT_C1 due to human activities, accounting for 33.8% and 17.1%, respectively (Figures 4b and 4c bar plot). As mentioned in the methodology, we draw primary results from NAT_C1, which represents multi-model means. However, the other NAT runs also exhibit significantly reduced area of extreme rainfall compared to the corresponding ALL runs. The consistency of these findings across the storms and simulations serves to enhance the reliability of the results. The increased average rainfall within a 400-km radius of these TCs in ALL compared to NAT_C1 is displayed in Figures 4d–4f. It further strengthens the conclusions about anthropogenic influence in TC-induced rainfall. A notable increase in rainfall is experienced within a 100–200 km radius. This hypothesis was further validated by analyzing other cluster simulations, which demonstrate stronger changes in NAT_C4 than others (Figure S5 in Supporting Information S1). Previous studies illustrate a non-uniform pattern of increase and decrease in rainfall, as observed in Figures 4d–4f (Fujiwara et al., 2025; Lee et al., 2023; Patricola & Wehner, 2018). Moreover, the time-averaged rainfall of each TC for all the simulations was examined (Figure S6 in Supporting Information S1) to ensure the noted increase in average rainfall is not just a re-orientation of the rain belt.

The heavy rainfall values in each scenario are compared by estimating the mean value of the 90th, 95th, 99th, and 99.9th percentile values in the entire period within a 300 km radius (Table 1). Results show that the values of heavy rainfall (95th to 99.9th percentile) were considerably high in ALL in complete TCs, statistically significant

**Table 1**
*Percentile Values of Heavy Precipitation*

| | Kyarr (mm 6 hr$^{-1}$) | | | Maha (mm 6 hr$^{-1}$) | | | Ockhi (mm 6 hr$^{-1}$) | | |
|---|---|---|---|---|---|---|---|---|---|
| Percentile | ALL | NAT | *p* value | ALL | NAT | *p* value | ALL | NAT | *p* value |
| 99.9 | **316.2 (9.12)** | **283.4 (13)** | **0.01** | **232.7 (14.01)** | **213.5 (2.93)** | **0.04** | 340.8 (8.69) | 328.1 (12.81) | 0.15 |
| 99 | **150.16 (4.15)** | **137.4 (2.31)** | **0.0** | **110.5 (3.26)** | **103.2 (2.7)** | **0.01** | **190.92 (5.66)** | **178.31 (4.22)** | **0.01** |
| 95 | **61.24 (1.14)** | **57.56 (1.93)** | **0.02** | **40.72 (1.64)** | **38.36 (0.7)** | **0.03** | **85.92 (0.74)** | **81.63 (1.42)** | **0.0** |
| 90 | 33.3 (1.37) | 32.22 (0.84) | 0.17 | 20.88 (1.38) | 19.71 (0.61) | 0.14 | **51.48 (0.69)** | **49.68 (0.69)** | **0.01** |

*Note.* Mean value of 90th, 95th, 99th and 99.9th percentile values of rainfall experienced inside a 300 km radius of each TC for ALL and NAT experiments. Values in parentheses indicate inter-ensemble standard deviation. The *p*-value was calculated by performing the Welch's *t*-test between ALL (5 members) and NAT (4 members). The cases of *p*-value less than 0.05 are indicated in bold.

at 5%. The sole exception to this is the 99.9th percentile of Ockhi, which has a confidence level of 85% only. Specifically, the 99.9th percentile values indicate a substantial increase in the intensity of heavy rainfall by 11.6%, 9%, and 3.9% in ALL compared to NAT for the TCs Kyarr, Maha, and Ockhi, respectively, with 95% confidence (except Ockhi; 85% confidence). To enhance the reliability of results, the median of the same samples is further compared with the Wilcoxon rank sum test, which is more robust than the *t*-test (Figure S7 in Supporting Information S1). The results obtained appear to be consistent with those presented in Table 1. It is evident that the intensity of extreme rainfall experienced in ALL is shown to be significantly larger than NAT, considering 95th, 99th and 99.9th percentile values in all the TCs at a level of 5%, with the exception of the 99.9th percentile of Ockhi (p-value = 0.15, 0.19 from Table 1 and Figure S7 in Supporting Information S1 respectively).

In summary, all the TCs exhibit increased mean rainfall within a 300 km radius in ALL compared to NAT. Notably, anthropogenic warming over the ARB leads to enhanced heavy rainfall and a larger fraction of the area experiencing extreme rainfall in ALL. These results are consistent with previous studies projecting increased TC rainfall rates globally under greenhouse warming (Kim et al., 2014, 2024; Knutson et al., 2013; Moon et al., 2023). For example, Villarini et al. (2014) reported an 18%–21% increase in TC-induced mean precipitation over the NIO in a 2 K warmer climate, while Knutson et al. (2015) and Liu et al. (2019) found an ∼11% increase under RCP4.5 in the far future (2081–2100). For extreme rainfall, using large-ensemble simulations, Yoshida et al. (2017) projected a ∼30% increase in lifetime maximum precipitation rates within 200 km of TCs under RCP8.5. Similar increases have been reported elsewhere, including an expansion of TC-induced extreme rainfall coverage from 1% to 18% over Texas (Emanuel, 2017) and a 17%–21% K$^{-1}$ increase in extreme rainfall intensity for TC Irma (Huprikar et al., 2023). Overall, these studies closely align with our findings on the magnitude and spatial shifts of TC-induced extreme rainfall over the ARB. Moisture convergence is expected to play a key role by enhancing the humidity of the TC vertical column and thus rainfall rates (Walsh et al., 2016). To further elucidate the underlying mechanisms, we analyze precipitation in relation to background environmental variables.

### 3.3. Clustering of Models

The comparison between the above-discussed clusters is a key aspect in this study for identifying the influence of different levels of anthropogenic forcings. The identical group formation when using the PC1 of MSE and SST against RH also justifies the above-described classification of clusters (Figures 1a and 1b). PC1 of both SST and MSE shows a significant inter-model correlation to PC1 of RH at the 5% level. The delta pattern is more prominently visible over the western parts of ARB than the eastern parts of the domain, irrespective of the variable (Figures 1c–1j). The bar plot inside each plot shows the area average of the delta pattern over ARB (black box in Figure 1c) and the whole domain. The EOF1 of SST and RH explains the variance (88% and 66%, respectively) in the entire domain (Figures S8a and S8c in Supporting Information S1). In a similar manner, larger SST and RH delta patterns are denoted by high PC1 (Figures S8e and S8g in Supporting Information S1). The conclusion drawn is that the basin-wide warming and humidification are indicated by larger PC1 values. Taking this into consideration, NAT_C2 and NAT_C3 are equally dominant by the SST delta. But within the framework of RH, NAT_C2 is more dominant than NAT_C3. However, NAT_C4 is the least dominant cluster in terms of both RH and SST. The previous studies found the RH as a stronger influencing factor than SST on the TC-induced rainfall and its areal extent (Hill & Lackmann, 2009, 2011; Kim et al., 2021). The impact of increased RH on the behavior

of TC, including the induced rainfall, can be checked by comparing NAT_C2 and NAT_C3, considering the observed contrast between them (delta RH of NAT_C3 > NAT_C2). The almost identical delta pattern of lower-tropospheric temperature (1000-700 hPa) in NAT_C2 and NAT_C3 supports this approach (Figure S2c–S2f in Supporting Information S1). Additionally, the cross-storm consistency of clustering and the legitimacy of comparing NAT_C2 and NAT_C3 are validated with the individual delta patterns applied to each TC after daily interpolation (described in methods) (Figures S9–S11 in Supporting Information S1). However, it should be noted that the track of TC Ockhi does not traverse the region with higher delta RH in NAT_C3, and its impact will be less evident in the case of Ockhi (Figures S10j and S10k in Supporting Information S1).

For a better understanding of anthropogenic warming patterns, the distribution of horizontal and vertical delta patterns across months is analyzed (Figures S12–S14 in Supporting Information S1). From the analysis of the NAT_C1 cluster, a greater degree of SST warming was exhibited in the months of November and December compared to October (Figure S12 in Supporting Information S1). In contrast, October has shown an enhanced RH pattern in comparison with other months (Figure S13 in Supporting Information S1). This contradiction needs to be addressed in future work. Nevertheless, Ockhi is the only TC that has been simulated in December, and its trajectory is entirely situated within the eastern Arabian Sea. Consequently, it is anticipated that there will be no impact on the model results. Similarly, the vertical structure of the domain is illustrated in Figure S14 of Supporting Information S1 for a better understanding of RH and T at different levels. A noticeable disparity in the pattern of RH and T was not observed across the months; however, the discrepancy between NAT_C2 and NAT_C3 on RH is well represented in all the months.

### 3.4. Background Variables

Here we examine the departure of background variables in ALL from NAT_C1 that are conducive to TC strengthening to identify the mechanism of increased rainfall previously detected. Due to human-induced warming, an additional latent heat (LH) release is detected within a 400 km radius of all the TCs (Figures 5a–5c). The 500 hPa vertical wind also shows an increase in ALL, which can boost atmospheric convection and cause additional rainfall, along with the LH release (Figures 5d–5f). We have prepared the scatter plot of change in vertical wind and rainfall to explain the spatial matching of vertical wind and corresponding rainfall anomaly (Figure S15 in Supporting Information S1). The figure shows points with predominantly positive rain anomalies and negative vertical wind anomalies (Figures S15e and S15h in Supporting Information S1). However, when all the points are considered, a positive correlation is observed, which is statistically significant at a level of 0.01%. This significant correlation is evident across all the TCs and simulations. However, it is important to note that the correlation value is too low. The phenomenon can be explained by the principle that when the vertical velocity is strong, it activates condensation and cloud formation, which subsequently leads to rainfall. It should be noted that, owing to the fact that the process is time-consuming, a time lag may be experienced. Furthermore, the spatial pattern of rainfall and vertical wind in the three stages of TC has been plotted (Figure S16 in Supporting Information S1) for the in-depth analysis of the pattern. The similarity in the pattern of rainfall and vertical wind in each stage of TC is distinctly visible. However, it is noteworthy that certain exceptional stages are also identified, such as stage 2 of Maha (Figures S16h and S16k in Supporting Information S1).

We further examine the relationship between TC-induced rainfall and the water vapor mixing ratio (WVMR) at 850 hPa following Lee et al. (2023). The results show that all the TCs exhibit a significantly wetter lower troposphere in ALL, which can contribute more water vapor to the mid-troposphere (Figures 5g–5i). Additionally, the ensemble runs NAT_C2, NAT_C3, and NAT_C4 also show the same pattern of decreased WVMR and LH compared to ALL, indicating the robust response (Figure S17 in Supporting Information S1). According to the well-known Clausius-Clapeyron relationship, the increase in WVMR is obvious as the atmosphere's capacity to hold water vapor increases by 7% per elevation of 1K temperature (Allen & Ingram, 2002; Held & Soden, 2006; Panthou et al., 2014). It is important to note that the NAT_C4, which displays the largest delta pattern, exhibits the highest departure of WVMR from ALL.

The inter-model correlation analysis of all the NAT runs establishes a significant relationship between WVMR and vertical wind against rainfall (Figures 6a and 6e). To confirm the robustness of the findings, we split the simulation time of each TC into three equal parts (Figure S1 in Supporting Information S1) and repeated the analysis for each period. Results show that the WVMR is significantly correlated to rainfall within a 300-km radius in all the periods except period 3 (Figures 6a–6d). ALL recorded higher rainfall than the NAT

10.1029/2025EF007294

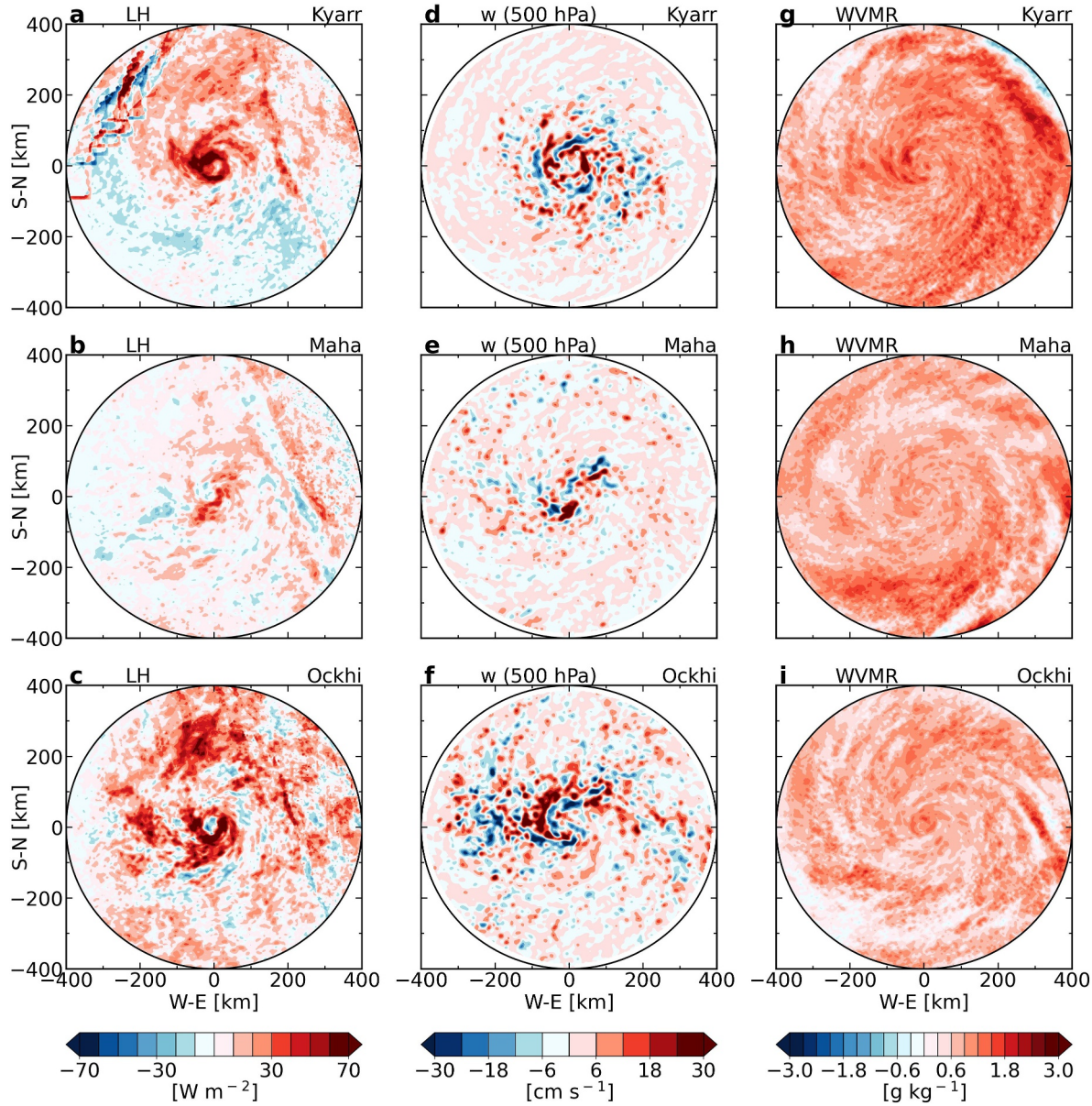


**Figure 5.** Response of LH, vertical wind, and water vapor mixing ratio (WVMR) to anthropogenic warming. (a, d, and g) Pattern of ALL minus NAT_C1 (time averaged) for variables LH, vertical wind, and WVMR within a 400 km radius in the entire period of TC Kyarr. (b, e, and h) and (c, f, and i) same as (a, d, and g) but for TC Maha and Ockhi, respectively.

simulations within a 300 km except Kyarr in period 3. Among the clusters, NAT_C2 and NAT_C4 exhibit the least and most departure from ALL, respectively (Figure 6a). This is well consistent with previous studies, which found mid-tropospheric moisture as a strong factor controlling the TC-induced rainfall (Lee et al., 2023; Liu et al., 2023; Liu & Wang, 2020). Similarly, the vertical wind exhibited a strong relationship with the rainfall within a 200-km radius during all storm periods, except period 2 (see Figures 6e–6h).

The additional evaporation from the sea surface inside the storm system is obviously seen in all the TCs due to anthropogenic warming. In fact, this enhanced evaporation is getting added to the WVMR (Cheng et al., 2012; Green & Zhang, 2013). The strong convection at the level of 500 hPa lifted the humid air to the mid-troposphere, which is called convective moistening (Bretherton et al., 2004; Fritz & Wang, 2013). The RH at the level of 400–600 hPa is found to be a strong influencing factor behind TC-induced rainfall (Liu et al., 2023). Using the parametric hurricane rainfall model, it is found that the rainfall inside the inner-core enhances with the increased

10.1029/2025EF007294

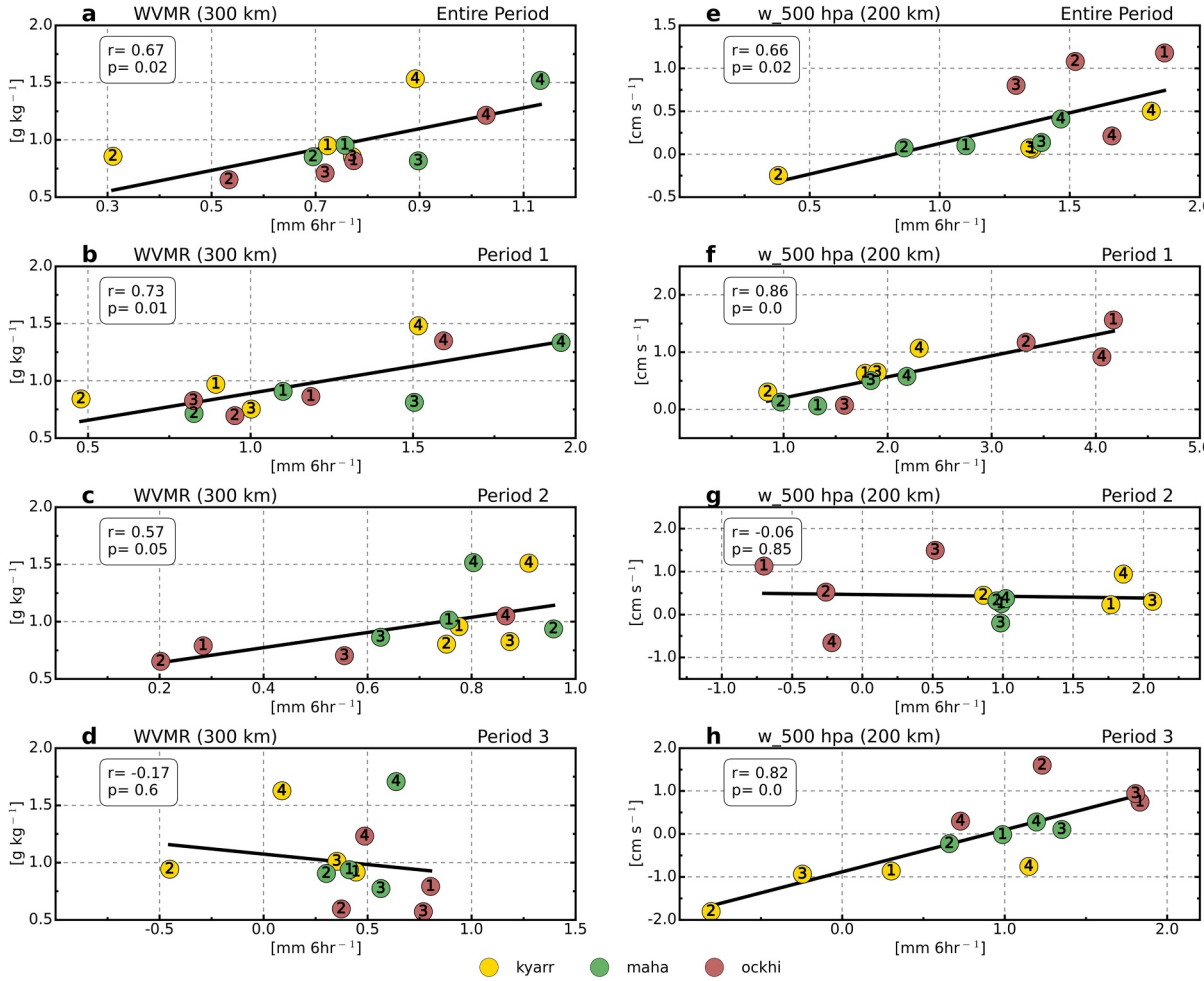


**Figure 6.** Relationship between rainfall and background variable responses. (a) Scatter plot of the rainfall and water vapor mixing ratio responses (ALL–NAT_C1) averaged within a 300 km radius in the entire period. Cluster numbers are represented inside each dot. Correlation coefficient (r) and corresponding *p* values are indicated. (b) Same as (a), but the scatter plot of vertical wind at 500 hPa and rainfall averaged inside a 200 km radius. (c, d), (e, f), (g, h) are the same as (a, b) but for periods 1, 2, and 3, respectively.

intensity of TC (Kim et al., 2022), whereas the rainfall received in the entire area of TC is impacted by the atmospheric moisture. These findings elucidate the mechanism through which human activity can lead to increased rainfall.

### 3.5. Effect of RH Change in Rainfall

Given the observation of an increase in RH over ARB (Abhiram Nirmal et al., 2023; Deshpande et al., 2021), it is essential to examine the impact of this increase on the rate of rainfall. To estimate it, a comparison was executed between the NAT_C2 and NAT_C3 clusters, with the relevant background variables. It is evident from Figure 7a that NAT_C2 experiences higher rainfall in TC Kyarr compared to NAT_C3, which is consistent with the larger delta RH of NAT_C3. At the same time, in TC Maha and Ockhi, this distinction is less visible (Figures 7b and 7c). However, the larger rainfall recorded in NAT_C2 compared to NAT_C3 is evident in all the TCs when checking the area-averaged rainfall of the entire period in a 300-km radius (Figure 6a). This corroborates the hypothesis—that additional rainfall experienced is attributed to increased RH. Along with the extra rainfall, LH and vertical wind exhibit a notable enhancement (Figures 7d–7i), which is complementary to the hypothesis, with more convection associated with elevated humidity. The relationship of LH to the TC intensity and rainfall rate has been well documented in previous research (Emanuel & Sobel, 2013; Jiang, 2012; Mittal et al., 2019; Zagrodnik

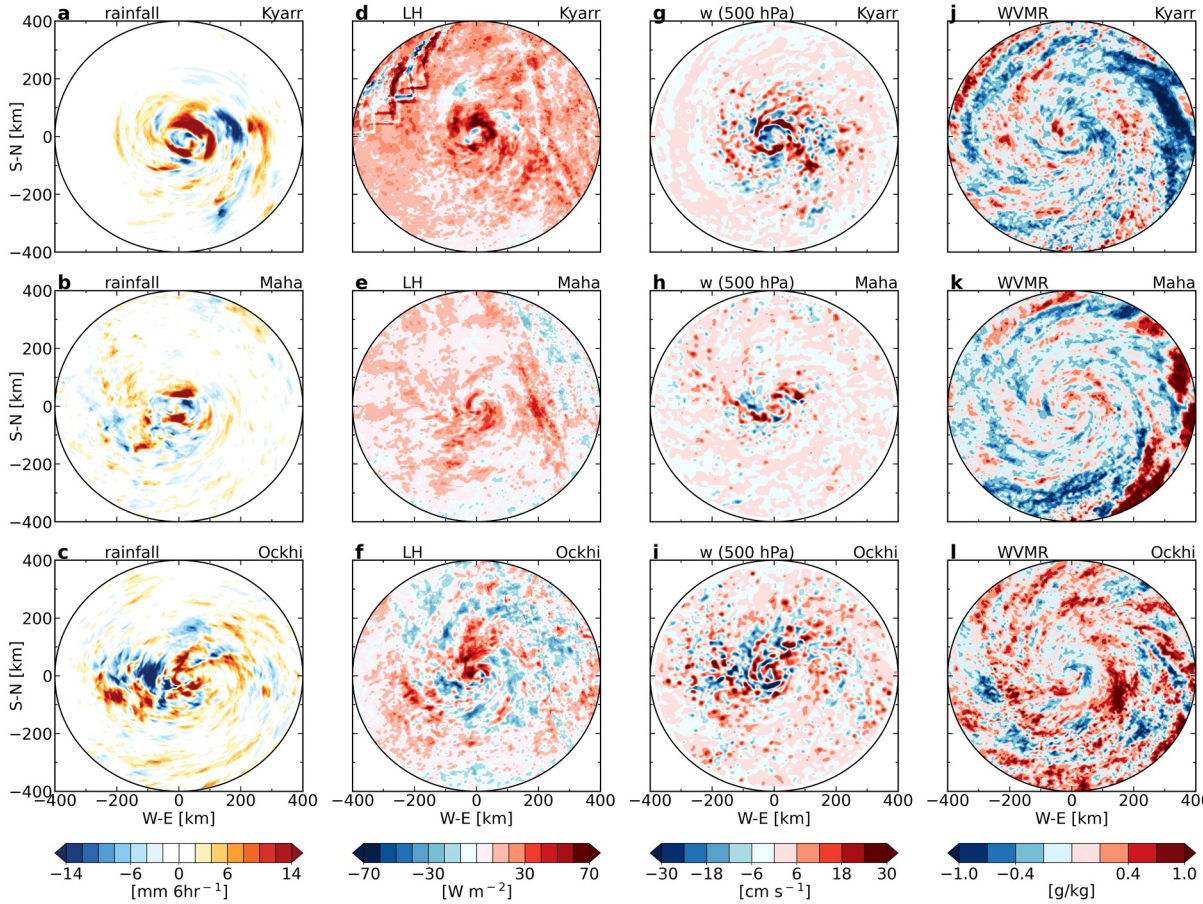


**Figure 7.** RH influence on TC rainfall and background variables. (a, d, g, and j) NAT_C2 minus NAT_C3 spatial patterns of rainfall, LH, vertical wind at 500 hPa, and water vapor mixing ratio averaged in the entire period for TC Kyarr. (b, e, h, and k) and (c, f, I, and l) same as (a, d, g, and j) but for TC Maha and Ockhi.

& Jiang, 2014). On the other hand, WVMR did not show this supportive disparity between the two clusters (Figures 7j–7l).

### 3.6. Change in the Vertical Structure of TC

The vertical structure of the TCs is also a key factor in the control of rainfall in TCs (Mukherjee & Ramakrishnan, 2022, 2023; Risi et al., 2023). Figure 8 presents an analysis of the change in the vertical structure of RH, WVMR, and the core temperature of ALL from NAT_C1, averaged over the entire period of TC evolution. The analysis reveals that TC Kyarr exhibits 2%–4% higher RH at the 600–200 hPa level (Figure 8a). This increased humidity in the region has been shown to result in increased rainfall during the landfall of a TC (Lin et al., 2015; Mittal et al., 2019). The findings are consistent with the analysis for all other TCs, increasing confidence (Figure S18 in Supporting Information S1). In the lower level (850–700 hPa), there is little RH difference near the center of the TC, and a large difference occurs 250 km away, where there is a small difference in TC precipitation (Figure 8a, Figure S18a and S18e in Supporting Information S1). The precipitation difference of the TC largely occurs near the center (Figures 4d–4f). Therefore, the decrease in RH in the lower level and the outer region would not have had a significant effect on the precipitation change. The departure of WVMR is higher in the lower troposphere, which can be due to additional LH and vapourization from the sea surface (Figure 8b). This finding is further confirmed through the analysis of area-averaged WVMR in the inner core (200 km) of Kyarr (Figure 8c). The increase in the core temperature of TC is attributable to anthropogenic warming, with a more pronounced rise above mid-troposphere (600-200 hPa). This departure of WVMR and RH in NAT_C1 is also consistent in other clusters, with a more noticeable pattern in NAT_C4 (Figures S19 and S20 in Supporting Information S1). The significant contribution of the well-noticeable warm and humid vertical

10.1029/2025EF007294

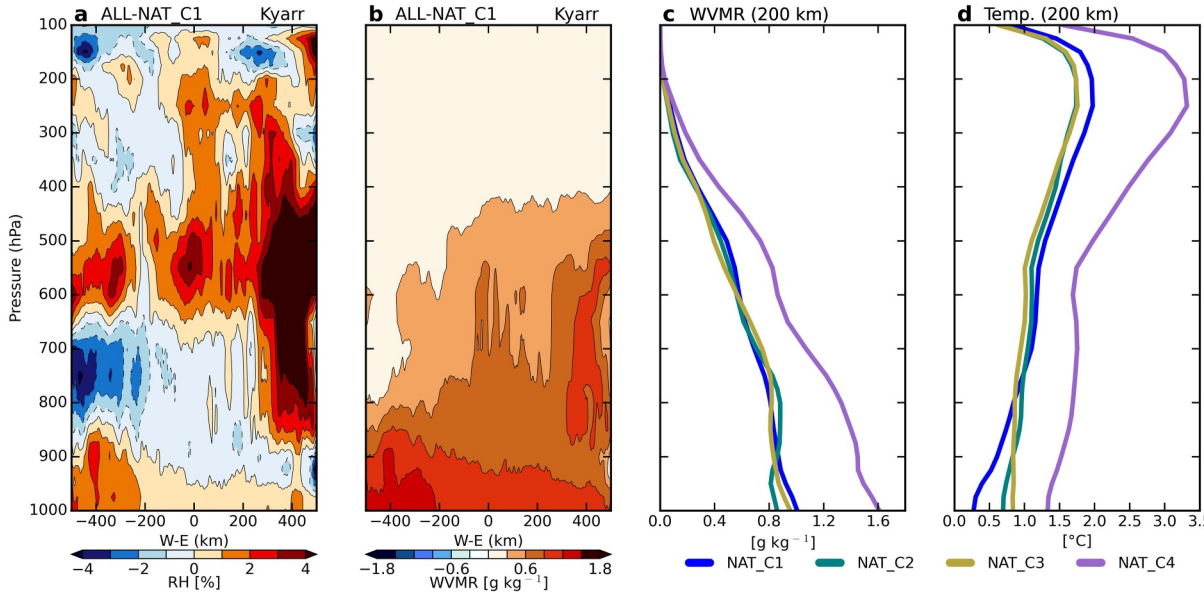


**Figure 8.** Response of TC vertical structure to anthropogenic warming. (a) ALL-NAT_C1 patterns of vertical distribution of RH with 500-km radius for TC Kyarr. In panels (b) same as (a) but with water vapor mixing ratio (WVMR) (1000–100 hPa). (c) The vertical structure of the area-averaged WVMR (ALL−NAT cluster) within a 200 km radius in the entire storm period. In panels (d) the same as (c), but for air temperature.

structure of TCs to more TC-induced rainfall is in accord with previous studies (Huang et al., 2025; Jiang, 2012; Mukherjee & Ramakrishnan, 2022, 2023).

## 4. Discussion and Conclusions

It is important to quantify the changes in the disruptiveness of individual historical TCs formed over ARB in a human-altered environment. In this study, we examined the changes that happened to the rainfall pattern and intensity of TCs using the WRF model with the PGW framework. The three most intense TCs formed over ARB after 2016 in the post-monsoon season were chosen for the simulations; Kyarr (2019), Maha (2019), and Ockhi (2017). The model was designed to enable the convection-permitting and spectral nudging schemes. In addition to all-forcing runs, we designed the natural-only forcing runs by removing the anthropogenic warming "delta" pattern from the real-world initial conditions. Further, clustering different delta patterns based on inter-model differences and comparing results among clusters aids in increasing the reliability of the results. Although future changes in TC intensity have been widely examined, quantitative attribution of TC-induced extreme rainfall to anthropogenic warming, particularly over ARB, remains largely unexplored. Previous PGW studies have primarily focused on TC track and intensity (Mittal et al., 2019; Ranji et al., 2022) or relied on a single model-derived warming pattern (Jyoteeshkumar Reddy et al., 2021). In contrast, this study provides a multi-model-based assessment of anthropogenic forcing on TC-induced rainfall and elucidates the underlying physical mechanisms by examining both the horizontal and vertical structure of TCs. Furthermore, we address a critical gap in the literature by offering a regional, risk-oriented perspective on cyclone impacts and the associated increase in flood hazards along the ARB coasts.

The model efficiently captures the track, intensity, and average rainfall within 300 km in all the simulations. From the comparison of ALL and NAT runs, it is evident that there is an additional amount of rainfall and extreme rainfall in ALL runs, which is significant and attributed to the anthropogenic forcings. The PDF and percentile values of rainfall display that the intensity of heavy rainfall is also shown to be substantially higher in ALL runs. More importantly, results from the cluster NAT_C1 (delta pattern representing multi-model means) indicate that if there were no anthropogenic warming, the area experiencing extreme rainfall would be less, about 16%–34% within a 300 km radius for TCs at 5% significance level. Similarly, the intensity of heavy rainfall is also increased by about 4%–12% due to human influence, with 95% confidence for Kyarr and Maha. The notable agreement between the ensemble simulations in both runs adds confidence to the results. Consistent with this increased

rainfall, ALL runs exhibit enhanced LH, vertical wind, and WVMR. The strong correlation between WVMR and vertical wind and the rainfall supports a physically consistent mechanism under anthropogenic warming: increased LH from the sea surface enhances low-level moisture, which is subsequently lifted into the mid-troposphere by deep convection, resulting in amplified rainfall. While these interpretations align with established thermodynamic relationships, the study provides a quantitative assessment of the magnitude and statistical significance of human influence on TC-induced extreme rainfall over ARB.

With the clustering of models, we designed experiments (NAT_C2 vs. NAT_C3) that can compare and analyze the impact of increased RH on the intensity of TC and TC-induced rainfall. From our analysis, we could observe distinguishably enhanced rainfall, LH, and vertical wind in Kyarr in response to this increased RH, although Maha and Ockhi do not exhibit this well-marked difference in rainfall. All the TCs show an enhanced pattern of high RH at the level 400–600 hPa in ALL compared to NAT within a 500 km radius. Additionally, the vertical structure of the TCs also shows the humidification to 400 hPa with a warmer core temperature in ALL.

We conclude that the historical intense TCs Kyarr, Maha, and Ockhi experienced a larger amount of rainfall and extreme rainfall with the support of more conductive background environments, due to anthropogenic warming. Future studies are warranted to address the caveats also remaining in this analysis. The limited number of models possessing both historical and hist-nat scenarios in CMIP6 pulls us back from designing a larger number of ensembles. In this study, we focus on the plausible impacts of human-induced changes in thermodynamic factors in the atmosphere influencing TC activity. It is necessary to incorporate dynamic factors such as vertical wind shear and vorticity as well into the PGW approach for a better understanding of the human impact on the destructiveness of TCs (Zhang & Tao, 2013). According to a recent study by Wang et al. (2025), the changes in the behavior of TCs in the future simulations are contingent on the changes in regional circulation (here, it is the north-west monsoon) and vertical wind shear. The results discussed above could be overestimated if dynamic factors actually inhibit it (e.g., increased vertical wind shear). Some studies simulate air-sea coupled processes that execute with WRF-ROMS (Chow et al., 2024; Warner et al., 2010) and WRF-NEMO (Parker et al., 2018; Samson et al., 2016). However, the present study focuses on the atmospheric processes and the impact of changing atmospheric boundary conditions. Therefore, the coupling of models is beyond the scope of this study. It is important to note that the increased amount of rainfall and extreme rainfall in the TCs that are passing close to land (like Ockhi and Maha) or making landfall have the potential to inflict substantial damage to the economies of the affected countries. Additionally, the coastal belt of ARB rim countries is projected to undergo a large increase in population density in the future with the SSP2 scenario (Harrington et al., 2018). The summary of these facts warns that the population living in the Arabian Sea rim countries will be more exposed to the highly devastating TCs like Ockhi and Maha due to anthropogenic climate forcings. The study calls on policymakers to develop targeted adaptation strategies aimed at coastal resilience and GHG emission mitigation strategies. Furthermore, it emphasizes the need for additional research on projected changes in TC landfalls considering different emission pathways.

## Conflict of Interest

The authors declare no conflicts of interest relevant to this study.

## Data Availability Statement

The WRF simulation data sets that support the results can be found in the repository on Zenodo via Pathaikara (2025). CMIP6 data are available at https://esgf-node.llnl.gov/projects/cmip6/. ERA5 hourly data are downloadable from Climate Data Store via Hersbach et al. (2020). Precipitation data from Tropical Rainfall Measuring Mission-3B42 version 7 (TRMM) and Integrated Multi-satellite Retrievals for GPM (IMERG) are downloadable via Huffman et al. (2007) and Hou et al. (2014), respectively.

**Acknowledgments**

This study was supported by Korea Meteorological Administration Research and Development Program under Grant RS-2024-00403386, National Research Foundation of Korea (NRF) grant funded by the Korean Government (MSIT) (NRF2021R1A2C3007366), and the Human Resource Program for Sustainable Environment in the 4th Industrial Revolution Society. We acknowledge the World Climate Research Programme, which, through its Working Group on Coupled Modeling, coordinated and promoted CMIP6. We thank the climate modeling groups for producing and making available their model output, the Earth System Grid Federation (ESGF) for archiving the data and providing access, and the multiple funding agencies who support CMIP6 and ESGF.

## References

Abhinav, R. S., Narvekar, J., Prasanna Kumar, S., & Francis, E. (2025). Is a warming northern Indian Ocean generating more tropical cyclones? *Journal of Operational Oceanography*, *18*(2), 105–122. https://doi.org/10.1080/1755876X.2025.2498272

Abhiram Nirmal, C. S., Abhilash, S., Martin, M., Sankar, S., Mohapatra, M., & Sahai, A. K. (2023). Changes in the thermodynamical profiles of the subsurface ocean and atmosphere induce cyclones to congregate over the Eastern Arabian Sea. *Scientific Reports*, *13*(1), 1–14. https://doi.org/10.1038/s41598-023-42642-9

Akhila, R. S., Kuttippurath, J., Rahul, R., & Chakraborty, A. (2022). Genesis and simultaneous occurrences of the super cyclone Kyarr and extremely severe cyclone Maha in the Arabian Sea in October 2019. *Natural Hazards*, *113*(2), 1133–1150. https://doi.org/10.1007/s11069-022-05340-9

Allen, M. R., & Ingram, W. J. (2002). Constraints on future changes in climate and the hydrologic cycle. *Nature*, *419*(6903), 224–232. https://doi.org/10.1038/nature01092

Bacmeister, J. T., Reed, K. A., Hannay, C., Lawrence, P., Bates, S., Truesdale, J. E., et al. (2018). Projected changes in tropical cyclone activity under future warming scenarios using a high-resolution climate model. *Climatic Change*, *146*(3–4), 547–560. https://doi.org/10.1007/s10584-016-1750-x

Behrangi, A., Song, Y., Pratama, G. N., Suwarman, R., Gede, D., Junnaedhi, A., et al. (2016). A global assessment of the timing of extreme rainfall from TRMM and GPM for improving hydrologic design. *Environmental Research Letters*, *11*(5), 054003. https://doi.org/10.1088/1748-9326/11/5/054003

Braun, S. A. (2006). High-Resolution simulation of Hurricane Bonnie (1998). Part II: Water budget. *Journal of the Atmospheric Sciences*, *63*(1), 43–64. https://doi.org/10.1175/JAS3609.1

Bretherton, C. S., Peters, M. E., & Back, L. E. (2004). Relationships between water vapor path and precipitation over the tropical Oceans. *Journal of Climate*, *17*(7), 1517–1528. https://doi.org/10.1175/1520-0442(2004)017<1517:RBWVPA>2.0.CO;2

Cheng, X., Fei, J., Huang, X., & Zheng, J. (2012). Effects of sea spray evaporation and dissipative heating on intensity and structure of tropical cyclone. *Advances in Atmospheric Sciences*, *29*(4), 810–822. https://doi.org/10.1007/S00376-012-1082-3/METRICS

Cho, W., Park, J., Moon, J., Cha, D. H., Moon, Y. M., Kim, H. S., et al. (2022). Effects of topography and sea surface temperature anomalies on heavy rainfall induced by Typhoon Chaba in 2016. *Geoscience Letters*, *9*(1), 1–18. https://doi.org/10.1186/S40562-022-00230-1/FIGURES/11

Chow, -C., Lau, C.-K., Lam, D.-S., Chan, C.-C., Leung, N.-C., Chow, C.-K., et al. (2024). WRF-ROMS-SWAN coupled model simulation Study: Effect of atmosphere–ocean coupling on sea level predictions under tropical cyclone and Northeast monsoon conditions in Hong Kong. *Atmosphere*, *15*(10), 1242. https://doi.org/10.3390/ATMOS15101242

Chu, J.-H., Sampson, C., Levine, A. S., & Fukada, E. (2002). The joint typhoon warning center tropical cyclone best-tracks, 1945–2000.

Delfino, R. J., Vidale, P. L., Bagtasa, G., & Hodges, K. (2023). Response of damaging Philippines tropical cyclones to a warming climate using the pseudo global warming approach. *Climate Dynamics*, *61*(7–8), 3499–3523. https://doi.org/10.1007/s00382-023-06742-6

Deser, C., Tomas, R. A., & Peng, S. (2007). The transient atmospheric circulation response to North Atlantic SST and sea ice anomalies. *Journal of Climate*, *20*(18), 4751–4767. https://doi.org/10.1175/JCLI4278.1

Deshpande, M., Singh, V. K., Ganadhi, M. K., Roxy, M. K., Emmanuel, R., & Kumar, U. (2021). Changing status of tropical cyclones over the north Indian Ocean. *Climate Dynamics*, *57*(11–12), 3545–3567. https://doi.org/10.1007/S00382-021-05880-Z/FIGURES/13

Durden, S. L. (2024). Evaluation of IMERG data over open ocean using observations of tropical cyclones. *Remote Sensing*, *16*(11), 2028. https://doi.org/10.3390/rs16112028

Emanuel, K. (1994). *Atmospheric convection*. Oxford University Press.

Emanuel, K. (2017). Assessing the present and future probability of Hurricane Harvey's rainfall. *Proceedings of the National Academy of Sciences of the United States of America*, *114*(48), 12681–12684. https://doi.org/10.1073/pnas.1716222114

Emanuel, K., & Sobel, A. (2013). Response of tropical sea surface temperature, precipitation, and tropical cyclone-related variables to changes in global and local forcing. *Journal of Advances in Modeling Earth Systems*, *5*(2), 447–458. https://doi.org/10.1002/JAME.20032

Emanuel, K. A. (1986). An air-sea interaction theory for tropical cyclones. Part I: Steady-state maintenance. *Journal of the Atmospheric Sciences*, *43*(6), 585–605. https://doi.org/10.1175/1520-0469(1986)043<0585:AASITF>2.0.CO;2

EM-DAT. (2008). EM-DAT: The international disaster database. Retrieved from https://doc.emdat.be/

Englehart, P. J., & Douglas, A. V. (2001). The role of eastern North Pacific tropical storms in the rainfall climatology of western Mexico. *International Journal of Climatology*, *21*(11), 1357–1370. https://doi.org/10.1002/JOC.637

Evans, J. L. (1993). Sensitivity of tropical cyclone intensity to sea surface temperature. *Journal of Climate*, *6*(6), 1133–1140. https://doi.org/10.1175/1520-0442(1993)006<1133:sotcit>2.0.co;2

Farneti, R., Stiz, A., & Ssebandeke, J. B. (2022). Improvements and persistent biases in the southeast tropical Atlantic in CMIP models. *npj Climate and Atmospheric Science*, *5*(1), 1–11. https://doi.org/10.1038/s41612-022-00264-4

Fritz, C., & Wang, Z. (2013). A numerical study of the impacts of dry air on tropical cyclone formation: A development case and a nondevelopment case. *Journal of the Atmospheric Sciences*, *70*(1), 91–111. https://doi.org/10.1175/JAS-D-12-018.1

Fujiwara, K., Takemi, T., & Mori, N. (2025). Impact of historical and future warming on heavy rainfall over eastern Japan induced by Typhoon Hagibis (2019) in dynamical downscaling simulations. *Natural Hazards*, *121*(2), 1819–1832. https://doi.org/10.1007/S11069-024-06875-9/FIGURES/10

Gillett, N. P., Shiogama, H., Funke, B., Hegerl, G., Knutti, R., Matthes, K., et al. (2016). The detection and attribution model intercomparison project (DAMIP v1.0) contribution to CMIP6. *Geoscientific Model Development*, *9*(10), 3685–3697. https://doi.org/10.5194/GMD-9-3685-2016

Gillett, N. P., Simpson, I. R., Hegerl, G., Knutti, R., Mitchell, D., Ribes, A., et al. (2025). The detection and attribution model intercomparison project (DAMIP v2.0) contribution to CMIP7. *Geoscientific Model Development*, *18*(14), 4399–4416. https://doi.org/10.5194/GMD-18-4399-2025

Gray, W. S. (1979). Hurricanes: Their formation, structure and likely role in the tropical circulation. https://api.semanticscholar.org/CorpusID:132807346

Green, B. W., & Zhang, F. (2013). Impacts of air–sea flux parameterizations on the intensity and structure of tropical cyclones. *Monthly Weather Review*, *141*(7), 2308–2324. https://doi.org/10.1175/MWR-D-12-00274.1

Gutmann, E. D., Rasmussen, R. M., Liu, C., Ikeda, K., Bruyere, C. L., Done, J. M., et al. (2018). Changes in hurricanes from a 13-Yr convection-permitting pseudo–global warming simulation. *Journal of Climate*, *31*(9), 3643–3657. https://doi.org/10.1175/JCLI-D-17-0391.1

Guzman, O., & Jiang, H. (2021). Global increase in tropical cyclone rain rate. *Nature Communications*, *12*(1), 1–8. https://doi.org/10.1038/s41467-021-25685-2

Harrington, L. J., Otto, F. E. L., Asselin, O., Leduc, M., & Paquin, D. (2018). Changing population dynamics and uneven temperature emergence combine to exacerbate regional exposure to heat extremes under 1.5°C and 2°C of warming. *Environmental Research Letters*, *13*(3), 034011. https://doi.org/10.1088/1748-9326/AAAA99

Hauser, M., Orth, R., & Seneviratne, S. I. (2017). Investigating soil moisture-climate interactions with prescribed soil moisture experiments: An assessment with the community Earth system model (version 1.2). *Geoscientific Model Development*, *10*(4), 1665–1677. https://doi.org/10.5194/GMD-10-1665-2017

Held, I. M., & Soden, B. J. (2006). Robust responses of the hydrological cycle to global warming. *Journal of Climate*, *19*(21), 5686–5699. https://doi.org/10.1175/JCLI3990.1

Hersbach, H., Bell, B., Berrisford, P., Hirahara, S., Horányi, A., Muñoz-Sabater, J., et al. (2020). The ERA5 global reanalysis. *Quarterly Journal of the Royal Meteorological Society*, *146*(730), 1999–2049. https://doi.org/10.1002/QJ.3803

Hill, K. A., & Lackmann, G. M. (2009). Influence of environmental humidity on tropical cyclone size. *Monthly Weather Review*, *137*(10), 3294–3315. https://doi.org/10.1175/2009MWR2679.1

Hill, K. A., & Lackmann, G. M. (2011). The impact of future climate change on TC intensity and structure: A downscaling approach. *Journal of Climate*, *24*(17), 4644–4661. https://doi.org/10.1175/2011JCLI3761.1

Hong, S. Y. (2010). A new stable boundary-layer mixing scheme and its impact on the simulated East Asian summer monsoon. *Quarterly Journal of the Royal Meteorological Society*, *136*(651), 1481–1496. https://doi.org/10.1002/QJ.665

Hong, S. Y., & Lim, J.-O. J. (2006). The WRF single-moment 6-Class microphysics scheme (WSM6). *Asia-Pacific Journal of Atmospheric Sciences*, *42*(2), 129–151.

Hou, A. Y., Kakar, R. K., Neeck, S., Azarbarzin, A. A., Kummerow, C. D., Kojima, M., et al. (2014). The global precipitation measurement mission. *Bulletin of the American Meteorological Society*, *95*(5), 701–722. https://doi.org/10.1175/BAMS-D-13-00164.1

Huang, J., Ma, Z., Liu, L., Li, X., & Jiang, T. (2025). Perspectives and challenges on the interaction between tropical cyclone precipitation and the ocean: A review. *Atmospheric and Oceanic Science Letters*, *18*(2), 100573. https://doi.org/10.1016/J.AOSL.2024.100573

Huffman, G. J., Adler, R. F., Bolvin, D. T., Gu, G., Nelkin, E. J., Bowman, K. P., et al. (2007). The TRMM multisatellite precipitation analysis (TMPA): Quasi-global, multiyear, combined-sensor precipitation estimates at fine scales. *Journal of Hydrometeorology*, *8*(1), 38–55. https://doi.org/10.1175/JHM560.1

Huprikar, A. S., Stansfield, A. M., & Reed, K. A. (2023). A storyline analysis of Hurricane Irma's precipitation under various levels of climate warming. *Environmental Research Letters*, *19*(1), 014004. https://doi.org/10.1088/1748-9326/AD0C89

Iacono, M. J., Delamere, J. S., Mlawer, E. J., Shephard, M. W., Clough, S. A., & Collins, W. D. (2008). Radiative forcing by long-lived greenhouse gases: Calculations with the AER radiative transfer models. *Journal of Geophysical Research*, *113*(D13), 13103. https://doi.org/10.1029/2008JD009944

Jayasekara, S., Ushiyama, T., Rasmy, M., & Kamae, Y. (2024). Investigation of tropical cyclones in the North Indian Ocean and the linkage to extreme weather events over Sri Lanka. *Atmosphere*, *15*(4), 390. https://doi.org/10.3390/ATMOS15040390

Jiang, H. (2012). The relationship between tropical cyclone intensity change and the strength of inner-core convection. *Monthly Weather Review*, *140*(4), 1164–1176. https://doi.org/10.1175/MWR-D-11-00134.1

Jiang, H., Liu, C., & Zipser, E. J. (2011). A TRMM-based tropical cyclone cloud and precipitation feature database. *Journal of Applied Meteorology and Climatology*, *50*(6), 1255–1274. https://doi.org/10.1175/2011JAMC2662.1

Jyoteeshkumar Reddy, P., Sriram, D., Gunthe, S. S., & Balaji, C. (2021). Impact of climate change on intense Bay of Bengal tropical cyclones of the post-monsoon season: A pseudo global warming approach. *Climate Dynamics*, *56*(9–10), 2855–2879. https://doi.org/10.1007/S00382-020-05618-3/METRICS

Kabir, R., Ritchie, E. A., & Stark, C. (2022). Tropical cyclone exposure in the North Indian Ocean. *Atmosphere*, *13*(9), 1421. https://doi.org/10.3390/ATMOS13091421/S1

Karami, S., & Khansalari, S. (2024). Analysis and simulation of three tropical cyclones with different paths. In *The Arabian Sea*. https://doi.org/10.21203/RS.3.RS-3718445/V1

Kikuchi, K., Wang, B., & Fudeyasu, H. (2009). Genesis of tropical cyclone Nargis revealed by multiple satellite observations. *Geophysical Research Letters*, *36*(6). https://doi.org/10.1029/2009GL037296

Kim, D., Ho, C.-H., Murakami, H., & Park, D.-S. R. (2021). Assessing the influence of large-scale environmental conditions on the rainfall structure of Atlantic tropical cyclones: An observational study. *Journal of Climate*, *34*(6), 2093–2106. https://doi.org/10.1175/JCLI-D-20-0376.1

Kim, D., Park, D.-S. R., Nam, C. C., & Bell, M. M. (2022). The parametric hurricane rainfall model with moisture and its application to climate change projections. *npj Climate and Atmospheric Science*, *5*(1), 86. https://doi.org/10.1038/s41612-022-00308-9

Kim, H. S., Vecchi, G. A., Knutson, T. R., Anderson, W. G., Delworth, T. L., Rosati, A., et al. (2014). Tropical cyclone simulation and response to CO2 doubling in the GFDL CM2.5 high-resolution coupled climate model. *Journal of Climate*, *27*(21), 8034–8054. https://doi.org/10.1175/JCLI-D-13-00475.1

Kim, Y. H., Lee, M., Min, S. K., Park, D. S. R., Cha, D. H., Byun, Y. H., & Heo, J. (2024). Global warming–induced warmer surface water over the East China Sea can intensify typhoons like hinnamnor. *Bulletin of the American Meteorological Society*, *105*(8), E1416–E1421. https://doi.org/10.1175/BAMS-D-23-0240.1

Knaff, J. A., Longmore, S. P., DeMaria, R. T., & Molenar, D. A. (2015). Improved tropical-cyclone flight-level wind estimates using routine infrared satellite reconnaissance. *Journal of Applied Meteorology and Climatology*, *54*(2), 463–478. https://doi.org/10.1175/JAMC-D-14-0112.1

Knutson, T. R., Sirutis, J. J., Zhao, M., Tuleya, R. E., Bender, M., Vecchi, G. A., et al. (2015). Global projections of intense tropical cyclone activity for the late twenty-first century from dynamical downscaling of CMIP5/RCP4.5 scenarios. *Journal of Climate*, *28*(18), 7203–7224. https://doi.org/10.1175/JCLI-D-15-0129.1

Knutson, T. R., Sirutis, J. J., Bender, M. A., Tuleya, R. E., & Schenkel, B. A. (2022). Dynamical downscaling projections of late twenty-first-century U.S. landfalling hurricane activity. *Climatic Change*, *171*(3), 1–23. https://doi.org/10.1007/S10584-022-03346-7

Knutson, T. R., Sirutis, J. J., Vecchi, G. A., Garner, S., Zhao, M., Kim, H. S., et al. (2013). Dynamical downscaling projections of twenty-first-century Atlantic hurricane activity: CMIP3 and CMIP5 model-based scenarios. *Journal of Climate*, *26*(17), 6591–6617. https://doi.org/10.1175/JCLI-D-12-00539.1

Kumar, S., Routray, A., Chawla, P. S., & Kalra, S. (2020). Simulation of intensity and track of tropical cyclones over the Arabian Sea using the weather research and forecast (WRF) modeling system with different initial conditions (ICs). *Techniques for Disaster Risk Management and Mitigation*, 77–84. https://doi.org/10.1002/9781119359203.CH6

Lan, Y. Y., Hsu, H. H., Tseng, W. L., & Jiang, L. C. (2022). Embedding a one-column ocean model in the community atmosphere model 5.3 to improve Madden-Julian oscillation simulation in boreal winter. *Geoscientific Model Development*, *15*(14), 5689–5712. https://doi.org/10.5194/GMD-15-5689-2022

Lauer, A., Zhang, C., Elison-Timm, O., Wang, Y., & Hamilton, K. (2013). Downscaling of climate change in the Hawaii region using CMIP5 results: On the choice of the forcing fields. *Journal of Climate*, *26*(24), 10006–10030. https://doi.org/10.1175/JCLI-D-13-00126.1

Lee, M., Min, S. K., & Cha, D. H. (2023). Convection-permitting simulations reveal expanded rainfall extremes of tropical cyclones affecting South Korea due to anthropogenic warming. *npj Climate and Atmospheric Science*, *6*(1), 1–12. https://doi.org/10.1038/s41612-023-00509-w

Leipper, D. F., & Volgenau, D. (1972). Hurricane heat potential of the Gulf of Mexico. *Journal of Physical Oceanography*, *2*(3), 218–224. https://doi.org/10.1175/1520-0485(1972)002<0218:HHPOTG>2.0.CO;2

Lin, I. I., Chen, C. H., Pun, I. F., Liu, W. T., & Wu, C. C. (2009). Warm ocean anomaly, air sea fluxes, and the rapid intensification of tropical cyclone Nargis (2008). *Geophysical Research Letters*, *36*(3). https://doi.org/10.1029/2008GL035815

Lin, Y., Zhao, M., & Zhang, M. (2015). Tropical cyclone rainfall area controlled by relative sea surface temperature. *Nature Communications*, *6*(1), 1–7. https://doi.org/10.1038/ncomms7591

Liu, L., & Wang, Y. (2020). Trends in landfalling tropical cyclone–induced precipitation over China. *Journal of Climate*, *33*(6), 2223–2235. https://doi.org/10.1175/JCLI-D-19-0693.1

Liu, M., Vecchi, G. A., Smith, J. A., & Knutson, T. R. (2019). Causes of large projected increases in hurricane precipitation rates with global warming. *npj Climate and Atmospheric Science*, *2*(1), 38. https://doi.org/10.1038/s41612-019-0095-3

Liu, T., Chen, Y., Chen, S., Li, W., & Zhang, A. (2023). Mechanisms of the transport height of water vapor by tropical cyclones on heavy rainfall. *Weather and Climate Extremes*, *41*, 100587. https://doi.org/10.1016/j.wace.2023.100587

Lonfat, M., Rogers, R., Marchok, T., & Marks, F. D. (2007). A parametric model for predicting hurricane rainfall. *Monthly Weather Review*, *135*(9), 3086–3097. https://doi.org/10.1175/MWR3433.1

Lyon, B. (2022). Biases in sea surface temperature and the annual cycle of greater Horn Of Africa rainfall in CMIP6. *International Journal of Climatology*, *42*(8), 4179–4186. https://doi.org/10.1002/JOC.7456

Marquet, P. (1993). Exergy in meteorology: Definition and properties of moist available enthalpy. *Quarterly Journal of the Royal Meteorological Society*, *119*(511), 567–590. https://doi.org/10.1002/QJ.49711951112

Matyas, C. J. (2010). Associations between the size of hurricane rain fields at landfall and their surrounding environments. *Meteorology and Atmospheric Physics*, *106*(3–4), 135–148. https://doi.org/10.1007/s00703-009-0056-1

Meinshausen, M., Vogel, E., Nauels, A., Lorbacher, K., Meinshausen, N., Etheridge, D. M., et al. (2017). Historical greenhouse gas concentrations for climate modelling (CMIP6). *Geoscientific Model Development*, *10*(5), 2057–2116. https://doi.org/10.5194/GMD-10-2057-2017

Michalek, A., Done, J. M., & Villarini, G. (2024). Future changes in regional tropical cyclone wind, precipitation, and flooding using event-based downscaling. *Earth's Future*, *12*(6), e2023EF004279. https://doi.org/10.1029/2023EF004279

Mittal, R., Tewari, M., Radhakrishnan, C., Ray, P., Singh, T., & Nickerson, A. K. (2019). Response of tropical cyclone Phailin (2013) in the Bay of Bengal to climate perturbations. *Climate Dynamics*, *53*(3–4), 2013–2030. https://doi.org/10.1007/S00382-019-04761-W

Mohan, P. R., Srinivas, C. V., & Venkatraman, B. (2022). Convection-permitting WRF simulations of tropical cyclones over the North Indian Ocean. *Pure and Applied Geophysics*, *179*(4), 1333–1363. https://doi.org/10.1007/S00024-022-02985-2/METRICS

Mohanty, U. C., Mohapatra, M., Singh, O. P., Bandyopadhyay, B. K., & Rathore, L. S. (2014). Monitoring and prediction of tropical cyclones in the Indian Ocean and climate change. *Monitoring and Prediction of Tropical Cyclones in the Indian Ocean and Climate Change*, 1–428. https://doi.org/10.1007/978-94-007-7720-0/COVER

Mohanty, U. C., Osuri, K. K., Tallapragada, V., Marks, F. D., Pattanayak, S., Mohapatra, M., et al. (2015). A great escape from the Bay of Bengal "Super Sapphire–Phailin" tropical cyclone: A case of improved weather forecast and societal response for disaster mitigation. *Earth Interactions*, *19*(17), 1–11. https://doi.org/10.1175/EI-D-14-0032.1

Mohapatra, M., & Sharma, M. (2025). Cyclone warning system in India: A journey of success over 25 years. *Weather and Forecasting*, *40*(6), 829–855. https://doi.org/10.1175/WAF-D-23-0188.1

Moon, J., Park, J., Cha, D.-H., & Moon, Y. (2021). Five-day track forecast skills of WRF model for the Western north Pacific tropical cyclones. *Weather and Forecasting*, *36*(4), 1491–1503. https://doi.org/10.1175/WAF-D-20-0092.1

Moon, M., Ha, K. J., Kim, D., Ho, C. H., Park, D. S. R., Chu, J. E., et al. (2023). Rainfall strength and area from landfalling tropical cyclones over the North Indian and western North Pacific oceans under increased CO2 conditions. *Weather and Climate Extremes*, *41*, 100581. https://doi.org/10.1016/J.WACE.2023.100581

Mori, N., Kato, M., Kim, S., Mase, H., Shibutani, Y., Takemi, T., et al. (2014). Local amplification of storm surge by super Typhoon Haiyan in Leyte Gulf. *Geophysical Research Letters*, *41*(14), 5106–5113. https://doi.org/10.1002/2014GL060689

Mukherjee, P., & Ramakrishnan, B. (2022). On the understanding of very severe cyclone storm Ockhi with the WRF-ARW model. *Environmental Research: Climate*, *1*(1), 015002. https://doi.org/10.1088/2752-5295/AC6ADB

Mukherjee, P., & Ramakrishnan, B. (2023). Investigation of unique Arabian Sea tropical cyclone with GPU-based WRF model: A case study of Shaheen. *Journal of Atmospheric and Solar-Terrestrial Physics*, *246*, 106052. https://doi.org/10.1016/J.JASTP.2023.106052

Murakami, H., Mizuta, R., & Shindo, E. (2012). Future changes in tropical cyclone activity projected by multi-physics and multi-SST ensemble experiments using the 60-km-mesh MRI-AGCM. *Climate Dynamics*, *39*(9–10), 2569–2584. https://doi.org/10.1007/S00382-011-1223-X/FIGURES/9

Murakami, H., Wang, Y., Yoshimura, H., Mizuta, R., Sugi, M., Shindo, E., et al. (2012). Future changes in tropical cyclone activity projected by the new high-resolution MRI-AGCM. *Journal of Climate*, *25*(9), 3237–3260. https://doi.org/10.1175/JCLI-D-11-00415.1

Najah, A., van der Merwe, R., & Al Shehhi, M. R. (2025). Review of tropical cyclones impacting the Western Arabian Sea and Oman. *Journal of Operational Oceanography*, *18*(1), 21–39. https://doi.org/10.1080/1755876X.2024.2444753

Nogueira, R. C., & Keim, B. D. (2010). Annual volume and area variations in tropical cyclone rainfall over the Eastern United States. *Journal of Climate*, *23*(16), 4363–4374. https://doi.org/10.1175/2010JCLI3443.1

Olschewski, P., & Kunstmann, H. (2024). Future projections of hurricane intensity in the southeastern U.S.: Sensitivity to different Pseudo-Global Warming methods. *Frontiers in Climate*, *6*, 1353396. https://doi.org/10.3389/FCLIM.2024.1353396

Olschewski, P., Sun, Q., Wei, J., Li, Y., Tian, Z., Sun, L., et al. (2024). A storyline-based approach towards changing typhoon intensities over the Pearl river Delta under future conditions using pseudo-global warming. *Hydrology and Earth System Sciences Discussions*, *2024*, 1–32. https://doi.org/10.5194/HESS-2024-95

Panthou, G., Mailhot, A., Laurence, E., & Talbot, G. (2014). Relationship between surface temperature and extreme rainfalls: A multi-time-scale and event-based analysis. *Journal of Hydrometeorology*, *15*(5), 1999–2011. https://doi.org/10.1175/JHM-D-14-0020.1

Parker, C. L., Bruyère, C. L., Mooney, P. A., & Lynch, A. H. (2018). The response of land-falling tropical cyclone characteristics to projected climate change in northeast Australia. *Climate Dynamics*, *51*(9–10), 3467–3485. https://doi.org/10.1007/S00382-018-4091-9/METRICS

Pathaikara, A. (2025). Global warming influences on intense tropical cyclones in the Arabian Sea: Convection-permitting model experiments [Dataset]. *Zenodo*. https://doi.org/10.5281/zenodo.17082303

Pathaikara, A., Lee, M., Min, S. K., An, S. I., Roxy, M. K., & Sooraj, K. P. (2025). Human contribution to atmosphere-ocean thermodynamic factors affecting the intense tropical cyclones over the Arabian Sea during the post-monsoon season. *Weather and Climate Extremes*, *48*, 100755. https://doi.org/10.1016/J.WACE.2025.100755

Patricola, C. M., & Wehner, M. F. (2018). Anthropogenic influences on major tropical cyclone events. *Nature*, *563*(7731), 339–346. https://doi.org/10.1038/s41586-018-0673-2

Pradhan, R. K., & Markonis, Y. (2023). Performance evaluation of GPM IMERG precipitation products over the tropical oceans using buoys. *Journal of Hydrometeorology*, *24*(10), 1755–1770. https://doi.org/10.1175/JHM-D-22-0216.1

Prakash, S., Mahesh, C., Gairola, R. M., & Pal, P. K. (2012). Comparison of high-resolution TRMM-Based precipitation products during tropical cyclones in the North Indian Ocean. *Natural Hazards*, *61*(2), 689–701. https://doi.org/10.1007/S11069-011-0055-7/FIGURES/8

Prakash, S., Ramesh Kumar, M. R., Mathew, S., & Venkatesan, R. (2018). How accurate are satellite estimates of precipitation over the north Indian Ocean? *Theoretical and Applied Climatology*, *134*(1–2), 467–475. https://doi.org/10.1007/S00704-017-2287-2/FIGURES/7

Ranji, Z., Zarifsanayei, A. R., Cartwright, N., & Soltanpour, M. (2022). Climate change impacts on tropical cyclones of the Arabian Sea: Projections and uncertainty investigations. *International Journal of Climatology*, *42*(10), 5121–5141. https://doi.org/10.1002/JOC.7523

Ribes, A., Qasmi, S., & Gillett, N. P. (2021). Making climate projections conditional on historical observations. *Science Advances*, *7*(4), 671–693. https://doi.org/10.1126/SCIADV.ABC0671

Ricciardulli, L., Howell, B., Jackson, C. R., Hawkins, J., Courtney, J., Stoffelen, A., et al. (2023). Remote sensing and analysis of tropical cyclones: Current and emerging satellite sensors. *Tropical Cyclone Research and Review*, *12*(4), 267–293. https://doi.org/10.1016/J.TCRR.2023.12.003

Risi, C., Muller, C., Vimeux, F., Blossey, P., Védeau, G., Dufaux, C., & Abramian, S. (2023). What controls the mesoscale variations in water isotopic composition within tropical cyclones and squall lines? Cloud resolving model simulations in radiative-convective equilibrium. *Journal of Advances in Modeling Earth Systems*, *15*(4), e2022MS003331. https://doi.org/10.1029/2022MS003331

Roxy, M. K., Saranya, J. S., Modi, A., Anusree, A., Cai, W., Resplandy, L., et al. (2024). Future projections for the tropical Indian Ocean. *The Indian Ocean and Its Role in the Global Climate System*, 469–482. https://doi.org/10.1016/B978-0-12-822698-8.00004-4

Samson, G., Masson, S., Durand, F., Terray, P., Berthet, S., & Jullien, S. (2016). Roles of land surface albedo and horizontal resolution on the Indian summer monsoon biases in a coupled ocean–atmosphere tropical-channel model. *Climate Dynamics*, *48*(5), 1571–1594. https://doi.org/10.1007/S00382-016-3161-0

Singh, V. K., Roxy, M. K., & Deshpande, M. (2020). The unusual long track and rapid intensification of very severe cyclone Ockhi. *Current Science*, *119*(5), 771. https://doi.org/10.18520/cs/v119/i5/771-779

von Storch, H., Langenberg, H., & Feser, F. (2000). A spectral nudging technique for dynamical downscaling purposes. *Monthly Weather Review*, *128*(10), 3664–3673. https://doi.org/10.1175/1520-0493(2000)128

Takayabu, I., Hibino, K., Sasaki, H., Shiogama, H., Mori, N., Shibutani, Y., & Takemi, T. (2015). Climate change effects on the worst-case storm surge: A case study of Typhoon Haiyan. *Environmental Research Letters*, *10*(6), 064011. https://doi.org/10.1088/1748-9326/10/6/064011

Villarini, G., Lavers, D. A., Scoccimarro, E., Zhao, M., Wehner, M. F., Vecchi, G. A., et al. (2014). Sensitivity of tropical cyclone rainfall to idealized global-scale forcings. *Journal of Climate*, *27*(12), 4622–4641. https://doi.org/10.1175/JCLI-D-13-00780.1

Wada, A. (2015). Verification of tropical cyclone heat potential for tropical cyclone intensity forecasting in the Western North Pacific. *Journal of Oceanography*, *71*(4), 373–387. https://doi.org/10.1007/S10872-015-0298-0

Wada, A., & Usui, N. (2007). Importance of tropical cyclone heat potential for tropical cyclone intensity and intensification in the Western North Pacific. *Journal of Oceanography*, *63*(3), 427–447. https://doi.org/10.1007/S10872-007-0039-0/METRICS

Walsh, K. J. E., Mcbride, J. L., Klotzbach, P. J., Balachandran, S., Camargo, S. J., Holland, G., et al. (2016). Tropical cyclones and climate change. *Wiley Interdisciplinary Reviews: Climate Change*, *7*(1), 65–89. https://doi.org/10.1002/WCC.371

Wang, B., & Zhou, X. (2008). Climate variation and prediction of rapid intensification in tropical cyclones in the western North Pacific. *Meteorology and Atmospheric Physics*, *99*(1–2), 1–16. https://doi.org/10.1007/S00703-006-0238-Z/METRICS

Wang, Y. Q., Satoh, M., Zhan, R. F., Zhao, J. W., & Xie, S. P. (2025). Tropical sea surface warming patterns and tropical cyclone activity. *A Review*, *42*(10), 1996–2017. https://doi.org/10.1007/s00376-025-5114-1

Warner, J. C., Armstrong, B., He, R., & Zambon, J. B. (2010). Development of a coupled ocean–atmosphere–wave–sediment transport (COAWST) modeling system. *Ocean Modelling*, *35*(3), 230–244. https://doi.org/10.1016/J.OCEMOD.2010.07.010

Webster, P. J. (2008). Myanmar's deadly daffodil. *Nature Geoscience*, *1*(8), 488–490. https://doi.org/10.1038/ngeo257

Wehner, M. F., Reed, K. A., Loring, B., Stone, D., & Krishnan, H. (2018). Changes in tropical cyclones under stabilized 1.5 and 2.0°C global warming scenarios as simulated by the community atmospheric model under the HAPPI protocols. *Earth System Dynamics*, *9*(1), 187–195. https://doi.org/10.5194/ESD-9-187-2018

Weller, E., Min, S. K., Cai, W., Zwiers, F. W., Kim, Y. H., & Lee, D. (2016). Human-caused indo-pacific warm pool expansion. *Science Advances*, *2*(7), e1501719. https://doi.org/10.1126/sciadv.1501719

Xiao-ting, F., Ying, L., Xiao-ting, F., Ying, L., Ai-min, L., & Long-sheng, L. (2020). Statistical and comparative analysis of tropical cyclone activity over the Arabian Sea and Bay of Bengal (1977–2018). *Journal of Tropical Meteorology*, *26*(4), 441–452. https://doi.org/10.46267/J.1006-8775.2020.038

Yang, M. J., Braun, S. A., & Chen, D. S. (2011). Water budget of Typhoon Nari (2001). *Monthly Weather Review*, *139*(12), 3809–3828. https://doi.org/10.1175/MWR-D-10-05090.1

Yang, Y., Qin, K., & Durden, S. L. (2024). Evaluation of IMERG data over open ocean using observations of tropical cyclones. *Remote Sensing*, *16*(11), 2028. https://doi.org/10.3390/RS16112028

Yoshida, K., Sugi, M., Mizuta, R., Murakami, H., & Ishii, M. (2017). Future changes in tropical cyclone activity in high-resolution large-ensemble simulations. *Geophysical Research Letters*, *44*(19), 9910–9917. https://doi.org/10.1002/2017GL075058

Yuan, S., Zhu, L., & Quiring, S. M. (2021). Comparison of two multisatellite algorithms for estimation of tropical cyclone precipitation in the United States and Mexico: TMPA and IMERG. *Journal of Hydrometeorology*, *22*(4), 923–939. https://doi.org/10.1175/JHM-D-19-0296.1

Zagrodnik, J. P., & Jiang, H. (2014). Rainfall, convection, and latent heating distributions in rapidly intensifying tropical cyclones. *Journal of the Atmospheric Sciences*, *71*(8), 2789–2809. https://doi.org/10.1175/JAS-D-13-0314.1

Zhang, F., & Tao, D. (2013). Effects of vertical wind shear on the predictability of tropical cyclones. *Journal of the Atmospheric Sciences*, *70*(3), 975–983. https://doi.org/10.1175/JAS-D-12-0133.1

Zhang, Q., Liu, B., Li, S., & Zhou, T. (2023). Understanding models' global sea surface temperature bias in mean state: From CMIP5 to CMIP6. *Geophysical Research Letters*, *50*(4), e2022GL100888. https://doi.org/10.1029/2022GL100888